Space: Science & Technology
A SCIENCE PARTNER JOURNAL

REVIEW ARTICLE

Structure and Formation Mechanism of Lunar Regolith

Liping Qin[1,2*], Zongyu Yue[3], Sheng Gou[3], Yingnan Zhang[1,2], Guangfei Wei[4], Ke Shi[5], Xuhang Zhang[6,7,8], and Bing Yang[1,2]

[1]State Key Laboratory of Lithospheric and Environmental Coevolution/Deep Space Exploration Laboratory, University of Science and Technology of China, Hefei 230026, China. [2]CAS Center for Excellence in Comparative Planetology, Hefei 230026, China. [3]Key Laboratory of Earth and Planetary Physics, Institute of Geology and Geophysics, Chinese Academy of Sciences, Beijing 100029, China. [4]Institute of Deep Space Sciences, Deep Space Exploration Laboratory, Hefei 230026, China. [5]Key Laboratory of Information System and Technology, Beijing Institute of Control and Electronic Technology, Beijing 100038, China. [6]State Key Laboratory of Lithospheric and Environmental Coevolution, Institute of Geology and Geophysics, Chinese Academy of Sciences, Beijing 100029, China. [7]Institute of Geology and Geophysics, Chinese Academy of Sciences, Beijing 100029, China. [8]College of Earth and Planetary Sciences, University of Chinese Academy of Sciences, Beijing 100049, China.

*Address correspondence to: lpqin@ustc.edu.cn

Citation: Qin L, Yue Z, Gou S, Zhang Y, Wei G, Shi K, Zhang X, Yang B. Structure and Formation Mechanism of Lunar Regolith. *Space Sci. Technol.* 2025;5:Article 0219. https://doi.org/10.34133/space.0219

Submitted 20 December 2023
Revised 7 April 2024
Accepted 24 September 2024
Published 9 April 2025

Lunar regolith is a thin layer of weakly cohesive detrital materials covering the lunar surface. Studies on returned lunar samples have revealed that the lunar regolith mainly consists of fragments of rocks, minerals, breccia, glasses, and agglutinates with a median grain size of ~40 to 800 μm. The lunar regolith was produced from the space weathering of lunar rocks, including the following processes: meteoritic bombardment, solar wind implantation, solar and galactic cosmic ray irradiation, and gardening. During space weathering, the maturity of the lunar regolith increases as the median particle size decreases, and specific minerals and structures (such as nano Fe^0) are produced. The chemical and isotopic compositions of the lunar regolith also change via interactions with solar wind and cosmic rays. Volatiles resulting from solar wind, asteroid impacts, and volcanic degassing can be preserved in the lunar regolith and redistributed to the lunar polar regions during micrometeorite bombardment. Cosmic radiation can produce nuclides through spallation and neutron capture reactions, thereby changing the isotopic compositions of the lunar regolith, which could reflect the gardening history of the lunar regolith. Thus, the lunar regolith carries massive information about the space weathering history, impacting processes, and the interior of the Moon. In this review, we discuss the progress that has been made toward understanding the composition, the lateral and vertical structure, and the formation processes of the lunar regolith, in particular, the progress that has been made after the Chang'E mission series.

Introduction

The lunar surface is covered by a layer of unconsolidated debris, including crystalline rock fragments, mineral fragments, breccias, agglutinates, and glasses. These complex mixtures are known as the lunar regolith. The thickness of the lunar regolith is 4 to 5 m in mare regions and approximately 10 to 15 m in the older highland regions. Analyses of lunar samples collected on the 6 Apollo missions indicated that particles larger than 1 cm in diameter accounted for approximately 70% of the total mass of the samples [1]. The remaining fine fraction (<1 mm) of lunar regolith is lunar soil. The formation and evolution of the lunar regolith consist of a long process of temperature fluctuation, micrometeorite bombardment, and solar wind particle injection. Therefore, lunar regolith is rich in information about interactions between the lunar surface environment and lunar rocks, making it a valuable subject for scientific research. Moreover, lunar regolith is also considered a critical target for engineering exploration and lunar resource exploitation [1].

In this review, we discuss the progress that has been made toward the understanding of the structure and composition of the lunar regolith, its formation mechanism, and the elemental and isotopic changes recorded during its formation. We will specifically focus on the new insights gained from the Chang'E missions.

The Composition and Structure of Lunar Regolith

Size distribution and particle population

Our current understanding of the lunar regolith has mainly been obtained from analyses of lunar samples and lunar meteorites.

Especially since Apollo returned lunar samples, the composition and particle size distribution of lunar soil have been extensively studied. The median grain size of the analyzed lunar samples mostly ranges from approximately 40 to 800 μm and averages between 60 and 80 μm [1–3]. For example, the median grain size of the Apollo 11 samples was 62 μm [4]. The latest Chang'E-5 (CE-5) lunar soil sample has a median grain size of 50 to 60 μm [5,6].

The particle size distribution of lunar regolith changes dynamically. Meteoritic bombardment plays a dominant role in regolith evolution [7]. With meteoritic bombardment, the lunar regolith is excavated, shattered, pulverized, melted, and mixed; these processes are accompanied by vertical overturning and burial, as well as horizontal material transport. The particle size of the lunar regolith decreases or increases respectively as the regolith is shattered or melted and welded. The grain size distribution of the local lunar regolith materials will reach a steady state when the agglutination process balances the comminution process [8]. Particle size analysis has revealed that the particle size distribution has bimodal characteristics for approximately half of the immature Apollo lunar soils, whereas the particle size distribution has unimodal characteristics for the mature and sub-mature Apollo lunar soils [5,8]. Other contributing mechanisms have also been suggested, such as electrostatic migration [9,10]. Owing to the local electric field, dust particles, particularly those smaller than 10 μm, are released by the lunar surface [11,12] and are then horizontally transported and deposited in allochthonous areas. Because it is limited by the lunar electric field, electrostatic migration only locally affects the particle size distribution of the lunar regolith within several centimeters. Vertically, the median grain size increases with depth overall, but it may decrease locally owing to discontinuities in the digging depth during multiple meteoritic bombardment processes.

In general, mature soils are fine-grained. However, in most lunar samples, the grain size distribution is unrelated to the exposure age [2]. The physical properties of lunar regolith, such as grain size, density, packing, and compressibility, are reasonably uniform. However, the exposure age influences the chemical composition of the lunar regolith: for example, its agglutinate content. Overall, the lunar regolith is composed of pristine rock fragments, mineral fragments, breccia fragments, glasses of various kinds, and unique lunar constructional particles called agglutinates. The heterogeneous distribution of lunar regolith leads to large variations in the composition among different sampling sites. In addition, the lunar regolith is an "open" system [7] because substantial quantities of foreign material, such as meteorites, micrometeorites, and solar wind particles, undergo considerable mixing in the lunar regolith. With an increased degree of comminution and melting, highly mature soil may significantly obscure the parent rock compositions. Compared with coarse and bulk lunar regolith, the fine part is rich in aluminum, sodium, and incompatible elements, and it is deficient in iron, magnesium, and titanium [13–15].

Micrometer- to millimeter-scale polymineralic rock fragments, mineral fragments, and breccia fragments retain the most information about the source rock. The lunar surface is mostly composed of mare basalt and anorthites; therefore, the rock fragments in the lunar regolith are mainly mare basalt fragments and highland feldspathic fragments. The finer lunar regolith particles have a more uniform composition and a higher glass content than the coarser ones [8]. The glass in lunar regolith can be divided into 2 types according to its origin: volcanic glass and agglutinitic glass. The average diameter of volcanic glass beads in lunar soil is generally <0.1 mm. Agglutinitic glass is typically rich in bubbles and nanometer metallic iron (nano Fe^0). The volcanic glasses are spheroidal, ellipsoidal, dumbbell-shaped, and teardrop-shaped and are generally similar in composition to the bulk regolith samples. However, agglutinitic glass is inhomogeneous and contains crystals of feldspar and ilmenite, abundant metal spheres, and possibly other minor constituents from exotic materials [16]. Depending on the type and abundance of the microscopic inclusions it contains, a variety of glass colors have been observed, including amber, deep red-brown, pale green, yellow, and colorless. Unique to surface soils of extraterrestrial bodies without atmosphere, such as the Moon and Mercury, agglutinates are the major constituent of the lunar regolith. In some mature regoliths, agglutinates may account for ≤60% of the soil by volume. Agglutinates are typically mid-sized and irregular in shape with mineral grains, lithic fragments, and glasses intermixed in varying proportions. Vesicles and fine metallic droplets are present in most glasses and agglutinates.

Vertical structure

Most of the returned lunar regolith is the Moon's boundary layer, which interacts with space and records space weathering and geological processes. The vertical structure and the global distribution of the lunar regolith provide critical information about lunar geological evolution and resources for future lunar exploration. Studying the thickness of lunar regolith, including in situ investigation and examination of returned samples, will help us understand the geological history of the Moon. The fine texture of regolith is also an excellent material for engineering construction and for in situ resource utilization by future lunar missions.

The shallow crustal structure of the Moon has been directly measured based on seismic experiments conducted during the Apollo missions. Active seismic experiments at the Apollo 14, 16, and 17 landing sites [17–19] and passive seismic experiments at the Apollo 11, 12, 14, 15, and 16 landing sites [20] were performed to measure the regolith thickness (see Table 1). Notably, Apollo 14 and Apollo 16 landed in non-mare areas where the regolith thickness values estimated from seismic refraction profiling were 8.5 and 12.2 m, respectively [21]. These values are apparently greater than those obtained from other Apollo missions that landed in mare areas. Coherent radar was also deployed from lunar orbit during the Apollo 17 mission to map subsurface structure to a depth of 1.6 km with a vertical resolution of ~400 m [22]. However, the coarse resolution was unable to estimate the regolith thickness globally.

Chang'E-3 (CE-3) was China's first lunar landing mission that touched the northern Mare Imbrium of the lunar nearside [23]. The lunar penetrating radar (LPR) onboard the Yutu rover is designed to investigate subsurface structures. The LPR consists of 2 channels: Channel 1 has a central frequency of 60 MHz that can penetrate to a maximum depth of 400 m with a resolution of 1 m [23]; Channel 2 has a central frequency of 500 MHz that can penetrate to a depth of >30 m with a resolution of 30 cm [24]. More than 9 subsurface layers have been identified, which suggests the presence of a complex geological process at the landing area [23]. The thickness of the regolith along the rover's transverse path revealed by LPR is approximately 4 to 6 m [25]. The Yutu-2 rover onboard the Chang'E-4 (CE-4) was the first to land in the Von Kármán crater on the far side of the Moon. Many researchers have used the LPR's observations to

Table 1. Regolith thickness at different locations on the Moon

Location	Thickness of regolith (m)	Technique	References
Apollo 11	4.4	Passive seismic experiment	[20]
Apollo 12	3.7	Passive seismic experiment	[20]
Apollo 14	8.5	Active seismic experiment	[250]
Apollo 15	4.4	Passive seismic experiment	[20]
Apollo 16	12.2	Active seismic experiment	[250]
Apollo 17	4.0	Active seismic experiment	[250]
CE-3	4.0–6.0	Lunar penetrating radar	[25]
CE-4	5.3–15.0	Lunar penetrating radar	[28]
CE-5	>3.0	Lunar regolith penetrating radar	[5]
Mare in average	5 (nearside)	Earth-based Arecibo radar observation	[41]
	5 (nearside)	Earth-based Arecibo radar observation	[38]
	4.5 (60°S–60°N)	Passive microwave observation	[37]
	12.6 (rock-free regolith)	Diviner rock abundance measurements	[44]
	6.3–6.9 (4 major maria of lunar nearside)	Simultaneous observations of LRS and LALT	[39]
Highland in average	12 (far side)	Earth-based Arecibo radar observation	[41]
	>10 (far side)	Earth-based Arecibo radar observation	[38]
	7.5 (60°S–60°N)	Passive microwave observation	[37]
	18.5 (rock-free regolith)	Diviner rock abundance measurements	[44]

understand the local subsurface structures (e.g., Chen et al. [26], Dong et al. [27], Feng et al. [28], and Li et al. [29]). Using the first 31 lunar days of LPR data, Chen et al. [26] suggested that the thickness of the regolith is in the range of 5.7 to 15.7 m with an average thickness of 11.8 m. This finding is in good accord with the work of Feng et al. [28], who estimated that the regolith thickness varies from ~5.3 to ~15.0 m based on the 500-MHz LPR data obtained along the rover path during the first 27 lunar days. However, Dong et al. [27] proposed that the thickness is constrained to ~12 m from LPR measurements obtained during the first 5 lunar days; this is greater than the impact crater morphology-derived value of ~2.5 to 7.5 m based on Lunar Reconnaissance Orbiter Camera (LROC) Narrow Angle Camera (NAC) images [30].

CE-5 is China's first lunar sample return mission, which successfully landed in the northeastern Oceanus Procellarum on 2020 December 1. To help guide the drilling process and to detect subsurface structures, the Lunar Regolith Penetrating Radar (LRPR) onboard the CE-5 has the ability to penetrate the subsurface to >2 m at a greater vertical resolution of 5 cm [5,31]. The regolith thickness was reported to be ≥2.5 m and to be dominated by fine particles with an abundance of rock fragments [31]. Combined with analyses of the real-time measurement of the bit pressure of the drill pipe, Li et al. [5] observed homogeneous lunar soil from the surface to a depth of 0.3 m. Beneath that layer, there is a 0.1-m-thick rock layer. At greater depths, between 0.7 and 1 m, the radar image indicates a hard texture, which is coincident with alternately increasing and decreasing bit pressure. Limited by the LRPR time window, the range of sounding images suggests that the regolith thickness at the CE-5 landing site is greater than 3 m and that it contains abundant rocks [5].

Crater morphology and statistics for crater size–frequency distribution are indirect but are the prevailing methods used to determine regolith thickness from orbital images [30,32–36]. For example, using high-quality LROC images and the morphology method [32], the thickness of the regolith was found to correlate well with the crater density (>20 km in diameter). An improved morphological method proposed by Di et al. [33] has been used to determine regolith thickness by measuring the distance between the ground surface and the floor of small, fresh craters. However, this method is highly dependent on the Sun incidence and topographic resolution.

The thickness of regolith on a global scale has also been investigated extensively using ground-based and orbital radar observations [37–41]. Using Earth-based 70-cm Aricebo radar data, Shkuratov and Bondarenko [41] and Fa and Wieczorek [38] retrieved lunar regolith thicknesses ranging from 2 to 17 m. However, this approach should be used cautiously when applied to regions with very high surface roughness. The Lunar Radar Sounder (LRS) onboard Japan's Kaguya spacecraft is designed to reveal the subsurface structure to a depth of ~5 km with a vertical resolution of 75 m owing to its low frequency of 5 MHz [40]. Combining the laser altimeter (LALT) onboard Kaguya with LRS, Kobayashi et al. [39] mapped the regolith depth at 4 major maria of the lunar nearside with a mean value of 6.3 to 6.9 m. However, the satellite-borne radar sounders have coarse resolution when measuring regolith thickness because of the inherent bandwidths and environmental clutter [27].

The Microwave Radiometer (MRM) onboard the Chang'E-1 is the world's first payload to detect near-surface microwave emission on the Moon. Based on the globally measured microwave brightness temperature dataset, Fa and Jin [37], Zhou et al. [42], and Gong and Jin [43] used different techniques to invert the global distribution of regolith thickness. The statistical results within the mid-low (60°S to 60°N) range revealed that the average thickness of regolith in maria is 4.5 m, whereas that in the highlands is 7.6 m [37]. Recently, a new technique using young and fresh craters corresponding to cold spots of infrared (IR) observations has been developed to determine the thickness of the lunar regolith [44] because larger craters can penetrate deeper into the regolith to excavate more rocks than smaller ones. That is, the rock abundance near cold spot craters can be used to determine the depth of excavation and rock-free regolith thickness. Based on the cold spot dataset within 50°N/S [45], Venkatraman and Paige [44] measured the lunar regolith thickness using Diviner (Lunar Radiometer Experiment onboard Lunar Reconnaissance Orbiter) rock abundance around cold-spot craters as the lower limit of depth. They estimated that the average rock-free regolith thickness is 12.6 m in the lunar mare and 18.5 m in the highlands—much thicker than the thickness determined by MRM inversion [37].

The Formation Mechanism of Lunar Regolith

Impact and gardening

Cratering is the chief factor that is responsible for the formation of lunar regolith. Impact craters are the predominant geomorphic features on the lunar surface, and their formation process can be divided into the following stages: contacting and compression, excavation, and modification [46]. When a meteorite makes contact with the surface of a planetary body, the contact and compression phase begins. After a super-speed meteorite impacts the surface of a planetary body, in a very short period of time, the contact area between the meteorite and the planetary body undergoes intense deformation and propagates outward in the form of a shock wave. The shock wave moves rapidly outward in the target and backward to the tail of the projectile, and a rarefaction wave is reflected back when the shock wave arrives at the tail of the projectile. The rarefaction wave propagates much faster in the compressed material and relieves the high pressure caused by the shock wave. When the head of the rarefaction wave catches the shock wave, the first stage of the impact process terminates. In this first phase, the occurrence area is relatively small, comparable in scale to the meteorite. However, the extremely high pressure in this area causes material to be crushed, liquefied, and even vaporized, and then to be ejected to surrounding regions. The lunar regolith's molten material primarily originates from this zone. The second stage begins immediately after the contact and compression stage ends, and a largely hemispherical shock wave propagates into the target, weakening as it expands and engulfs more material. This shock wave and the following rarefaction set target material in motion, and an ejecta curtain forms to excavate a cavity during this stage. At the end of this phase, a bowl-shaped transient crater is formed. In the third stage, because of gravitational instability, some material on the rim and walls of the transient crater slides to the crater bottom, and a breccia lens is produced in the crater's center [46–49].

The formation and evolution of the lunar regolith are closely related to the impact. The agglutinate material and molten glass in lunar regolith are primarily a result of the ultrahigh pressure during the contact and compression stage. In the subsequent excavation process, deep material can be excavated and spattered to the surface, and some original surficial material can be buried in the final modification process. In previous studies, the above-mentioned overturning and mixing processes of surficial material caused by impact is defined as impact gardening [7,50]. Notably, meteorite impact information has been mostly recorded in lunar surface materials [51–53] because there is no atmosphere on the Moon, and little tectonic activity occurred in the last 3.0 Ga [54]. Therefore, understanding the impact cratering process and the closely related gardening process is necessary in researching lunar impact history, lunar surface rock fragmentation, the lunar regolith formation process, and the surficial structure of the Moon [55–57].

Since the first high-resolution image of the Moon was sent by Ranger 7 in 1964 (https://www.jpl.nasa.gov/missions/ranger-7), the lunar regolith formation process and the related gardening process have been widely studied. A primary method for quantitatively studying the aforementioned processes involves establishing models for the formation and evolution of lunar regolith. In 1973, Oberbeck et al. [58] developed a Monte Carlo model to describe impact events and to analyze the relationship between the growth of lunar regolith and impact events. This approach has been widely utilized and continuously refined, for example, by Quaide and Oberbeck [59] and Hörz [60]. Gault et al. [7] introduced an innovative model for the mixing of the weathering layer, also known as the surficial regolith layer, wherein the impact flux is assumed to follow a Poisson probability distribution. Building upon this foundation, Gault et al. [7] examined the likelihood of an impact event affecting a point at a specific depth and calculated the rate of overturning of lunar regolith at various depths and time intervals. Subsequently, Arnold [50], Fischer and Pieters [61], and Li and Mustard [62] delved deeper into this model, examining the intricate influence of the impact gardening phenomenon on the spatial arrangement of lunar regolith. Recent advancements in computing technology and the ongoing progress in understanding crater formation and degradation have led to significant enhancements in the lunar regolith evolution model. Richardson [63] introduced the Cratered Terrain Evolution Model (CTEM), offering a comprehensive investigation into the formation and vanishing of impact craters and their ejecta. Building upon the CTEM, Huang et al. [64] incorporated a regolith transport model to examine the impact transport and mixing dynamics at the lunar mare/highland interface. Costello et al. [57] updated the classical model proposed by Gault et al. [7] by utilizing the novel research results of impact flux and crater scaling law. Regarding impact melts distribution, Liu et al. [65] analyzed the effects of the long-term gardening process for 3 impact basins (Serenitatis, Crisium, and Imbrium). These investigations have significantly advanced our understanding of the impact gardening mechanism and of the evolutionary patterns of lunar regolith. Nonetheless, owing to the limited availability of necessary datasets, early studies were primarily focused on the spatial arrangement modeling of lunar regolith and lacked confirmation from in situ high-resolution stratigraphic data.

On 2019 January 3, China's CE4 probe successfully achieved a soft landing in the Von Kármán crater inside the South Pole–Aitken Basin on the far side of the Moon [53,66], and the onboard LPR has provided information about the lunar regolith structure underneath. Recent studies revealed that the material up to the depth of dozens of meters underneath the CE4 landing area is mostly the ejecta from the Finsen crater, and the geological age of the Finsen crater is approximately 3.5 Ga [67]. With the "CraterTools" add-in in ArcGIS [68], we delineated 2,049 craters with diameters between 5.0 and 317.6 m in the

1-km^2 area around the CE4 landing point in the LROC NAC image at a spatial resolution of 0.89 m/pixel. In addition, to evaluate the influence of the impact events outside the research area, studies identified a total of 6,093 impact craters within 50 km × 30 km around the landing site based on mosaic images [69]. These impact events could be used in subsequent calculations of lunar regolith thickness, excavation depth, overturning times, and grain size.

To quantitatively evaluate the influence of the formation processes of these craters on the formation and evolution of lunar regolith in this region, we used the empirical equations to calculate the ejecta thickness inside and outside the craters [70–72], to calculate the depth of the transitional crater as a rotating paraboloid [46], and to calculate the fragment size [46,73] for a single impact event. Next, we simulated these impact events within the study area using the Monte Carlo method, ensuring compliance with the chronology function and the production function [74,75]. Notably, the lunar regolith is also affected by the continuous effects of material rupture caused by large temperature differences on the lunar surface, lunar earthquakes, and micrometeorite bombardments. These effects are collectively considered as the degradation of terrain, which also contributes to the evolution of lunar regolith and can be described by the diffusion equation [63,76]. This model has been included in our studies, and the terrain diffusion rate has been set at 5.5 m^2/Myr (million years) [77]. The lunar regolith thickness and distribution have been calculated at every 0.01 Ga. We report that (a) the formation of the lunar regolith is mainly determined by large-scale impact events, whereas small-scale impact events have a significant effect on the mixing and overturning of shallow lunar regolith; (b) the grain size of the regolith material does not strictly increase with the depth, and some smaller grains can be found at the greater depths; and (c) in the initial 0.5 Ga, the impact flux was very high, and the spatial distribution of lunar regolith thickness was determined rapidly at that time. The simulated lunar regolith structure is largely consistent with the observations by the LPR onboard CE4, although our results revealed much more details on the lunar regolith in this area [78]; e.g., Fig. 1 shows the results on regolith thickness and grain size at different ages.

Space weathering

The surface of airless planetary bodies, such as the Moon, is continuously and permanently modified, either physically, chemically, or spectrally, by micrometeorite impacts, solar wind particles, and galactic cosmic rays [79]. The term “space weathering” is used to encompass all of the gradual alteration processes caused by interactions between the surface regolith and the harsh space environment [79]. The ubiquitous space weathering processes on the lunar surface strongly affect the optical properties of the surface regolith: for example, causing the visible and near-infrared (NIR) reflectance to become appreciably dark, exhibiting a reddened continuum, and even nearly completely suppressing diagnostic absorption features [79]. In addition to the Moon, similar spectral alteration phenomena due to space weathering have also been reported for Mercury [80], Phobos [81], and various asteroids [82–85].

Optical alterations on the Moon are mainly caused by the gradual creation and accumulation of submicroscopic metallic iron (SMFe), including both nanophase (<33 nm in size) and microphase (>33 nm in size) metallic iron, also known as npFe^0 and μpFe^0. Studies of lunar samples revealed that nanophase particles deposit on the glassy rims of regolith particles and agglutinates, whereas microphase particles occur only within agglutinates [86–90]. These SMFe particles are usually formed by the in situ reduction and/or evaporative re-deposition of iron in silicates such as olivine or pyroxene in the lunar regolith during the bombardment of high-energy particles (e.g., hydrogen in solar wind) or micrometeorites [91]. However, after measuring the valence states of iron and observing the copresence of SMFe and Fe^{3+} in an amorphous mixture of olivine on a fine-grained CE-5 sample, Li et al. [92] reported that a disproportionation reaction of Fe^{2+} during micro-impacts can also generate SMFe particles. This finding provides a novel perspective on weathering mechanisms in regions or bodies that do not experience a strong solar wind component, such as permanently shadowed areas or outer solar system bodies. Smaller SMFe particles (<10 nm in diameter) greatly redden spectra in the visible (VIS) wavelengths while leaving the NIR region largely unaffected. Larger particles (>40 nm in diameter) darken spectra across the VIS/NIR range with little change in the overall shape of the continuum, while intermediate particles affect spectra in distinct patterns that vary with total iron abundance [88,89,93]. In addition to SMFe particles, amorphous layers, vesicles, and radiation tracks are also products of space weathering [79,94].

The lunar regolith has already been remotely observed by orbiters, measured in situ by rovers, and sampled by crewed/uncrewed spacecraft. Therefore, the physical properties, chemical composition, and spectral features of the regolith are well-studied and have been thoroughly characterized in the laboratory, particularly samples from the Apollo, Luna, and CE-5 missions. Observations of the structure and composition of Apollo-returned lunar regolith grains that were obtained using aberration-corrected scanning transmission electron microscopy (STEM) show a number of unexpected phases present in the grains, such as oxidized iron-rich nanoparticles [95]. Utt et al. [96] used spatially resolved near-field spectroscopy in the mid-infrared (MIR) to study the spectral effects of space weathering over a depth of 500 nm in Apollo-returned lunar regolith grains; their findings support a connection between microstructural/chemical changes and MIR effects in weathered lunar regolith. Yang et al. [97] performed a detailed microscale spectral survey of CE-5-returned lunar regolith grains and reported that the NIR bands are more susceptible than the MIR bands to space weathering effects. Observations of a single basaltic clast from another CE-5 sample obtained using scanning electron microscopy and transmission electron microscopy (TEM) analysis revealed phase-dependent effects on space weathering [94]: All mineral phases have a vapor deposit layer, whereas the microscopic textures of the solar wind irradiation-damaged zone are host-mineral-dependent; SMFe particles are spherical in the amorphized zone of pyroxenes, elongated in ilmenite, and irregular on the jagged surface of iron sulfide, but are not found in Fe-poor merrillite; vesicles were observed in the damaged zone of both ilmenite and merrillite but had different shapes [94].

Understanding space weathering processes is vital for deciphering remotely sensed data from previous, ongoing, or future missions to any airless planetary bodies. Simulations of micrometeorite bombardment and solar wind irradiation in the laboratory are valid means for studying weathering processes. For example, Sasaki et al. [98] simulated micrometeorite impacts by performing laser irradiation on pellet samples of olivine, pyroxene, and anorthite. Measurements of reflectance showed

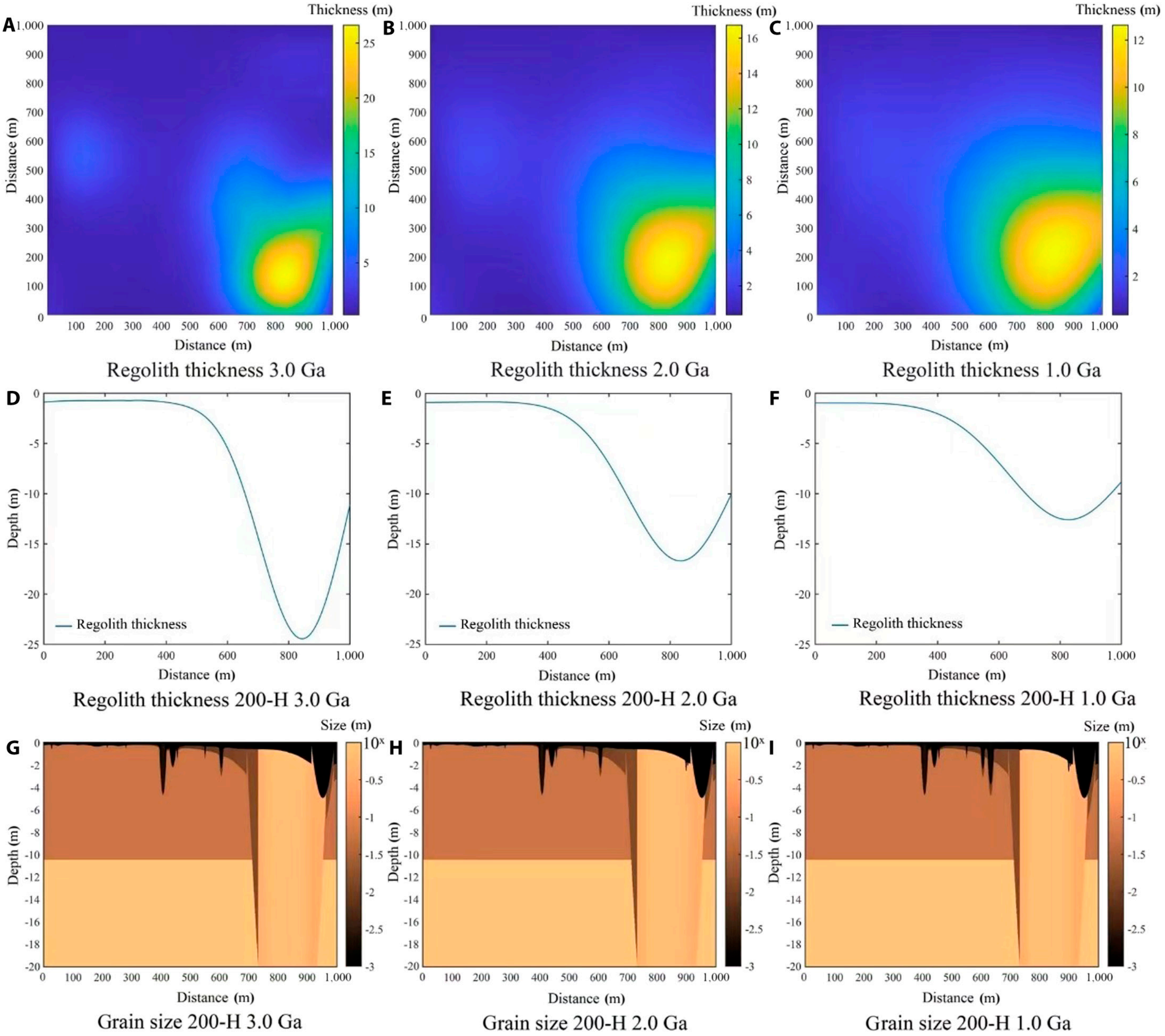

Regolith thickness 3.0 Ga

Regolith thickness 2.0 Ga

Regolith thickness 1.0 Ga

Regolith thickness 200-H 3.0 Ga

Regolith thickness 200-H 2.0 Ga

Regolith thickness 200-H 1.0 Ga

Grain size 200-H 3.0 Ga

Grain size 200-H 2.0 Ga

Grain size 200-H 1.0 Ga

Fig. 1. Evolution of lunar regolith in the CE4 landing area. (A), (B), and (C) show the spatial distribution of lunar regolith thickness at 3.0, 2.0, and 1.0 Ga, respectively; (D), (E), and (F) are profiles of lunar regolith thickness at the corresponding time along the horizontal line of $y = 200$ m; (G), (H), and (I) are profiles of lunar regolith grain size at the corresponding time along the horizontal line of $y = 200$ m. The units are all in meters. Note that the vertical scales are zoomed to 0 to 25 m scale in (D) to (I).

significant reddening, and the reduction of spectra was much larger in the visible region than in the NIR region. TEM observations revealed that $npFe^0$ are widely spread in rim regions of irradiated olivine grains; however, no trace of structural change was observed in irradiated olivine crystal samples, suggesting that the presence of regolith-like surface is essential for effective space weathering on asteroids. Matsuoka et al. [99] simulated micrometeorite bombardments on the surfaces of C-type asteroids using low-energy pulsed-laser irradiation experiments on chondrite samples, which resulted in spectral flattening and water absorption band suppression. Weber et al. [100] studied space weathering effects caused by micrometeorite bombardments using pulsed intense IR laser-irradiated samples and observed reductions in albedo and in the reflectance of characteristic Reststrahlen bands and an increase of the transparency feature. Marchi et al. [101] conducted ion irradiation experiments on multiple samples that produced reddening and darkening of reflectance spectra. Analysis of the spectral features of asteroids and meteorites with similar mineralogy but different distributions of spectral slopes suggests that these differences are caused by solar wind irradiation-triggered space weathering [101]. Loeffler et al. [102] studied the effects of ion irradiation on olivine both spectrally and chemically. The observed changes in reflectance, in particular the reddening slope, are correlated with the amount of metallic iron formed by ion impact. Moreover, the slower metallization rate of the powder when compared to that of the sectioned rock was proposed to be a consequence of redeposition of sputtered material [102]. Fulvio et al. [103] performed irradiation experiments with various ions and energies on different eucrites and observed the spectral alterations, specifically the progressive reddening and darkening of the irradiated samples. The findings from these simulations indicate that space weathering processes strongly affect the optical properties of the lunar regolith and must be seriously considered when analyzing remotely sensed data.

Space weathering processes result in the accumulation of SMFe in the lunar regolith over time until a steady-state equilibrium is reached as long as immature material is not excavated by an impact [56]. Consequently, SMFe abundance is a critical indicator for evaluating the degree of maturity of the regolith. An accuracy-and-spatial-resolution-improved space weathering map of the lunar surface [104] shows that the SMFe abundance is qualitatively similar to the optical maturity since fresh craters and their rays are the most apparent feature. Wang et al. [105] determined the SMFe abundance (0.368 wt.%) in regolith minimally disturbed by the CE-3 rocket exhaust and inferred a ferromagnetic resonance intensity normalized to total iron (Is/FeO) maturity index of ~53, indicating that the regolith is sub-mature. Spectroscopic measurements and optical modeling indicated that the SMFe abundance varies with distance from the landing site and depth from the uppermost surface; in other words, the natural uppermost surficial regolith is more weathered than the regolith underneath revealed by the rocket exhaust [105]. Gou et al. [106] determined the SMFe content (0.32 ± 0.06 wt.%) in the regolith at the CE-4 landing site and obtained a maturity index of 82 ± 15, suggesting that the Finsen Crater ejecta-sourced regolith is mature. Wu et al. [107] estimated the concentration of SMFe (0.14 wt.%) in the regolith at the CE-5 landing site and qualitatively assessed the regolith to be sub-mature. Unlike the phenomenon observed at the CE-3 landing site, the surficial regolith and the underlying centimeter-depth layer exhibit similar maturity, indicating that the upper few centimeters of lunar regolith have been substantially churned, and the disturbance from the rocket exhaust did not affect regolith maturity [107].

Inventory of Volatiles in Lunar Regolith

Water and other volatile elements significantly affect the melting temperatures of silicates and the fractional crystallization of magma. Therefore, the water content of the moon may play a key role in both the evolution of the lunar magma ocean (LMO) and in later volcanic activities of the lunar mantle. Moreover, water is a crucial resource for further exploration of the Moon. Early perspectives suggested that a substantial amount of water and other volatile components escaped during the Moon-forming giant impact [108], resulting in a relatively dry Moon [1]. This hypothesis was supported by the absence of water-bearing minerals and the generally low abundance of volatiles in lunar samples [1]. However, thanks to the development of remote sensing techniques, several studies have confirmed the presence of water on the lunar surface by analyzing IR spectroscopy data from the Chandrayaan-1, Deep Impact, and Cassini missions [109–112]. Subsequent lunar-impacting experiments performed by the Chandrayaan-1 and LCROSS missions confirmed that the permanently shadowed regions of lunar craters contain water ice and other volatile components [113–116]. The amount of water ice in the lunar regolith from permanently shadowed regions could be at least 0.5 to 4.0 wt.% [117]. Furthermore, the presence of water was discovered not only in polar regions but also in highland areas at lower latitudes [111]. Water in the lunar soil is present in the form of structurally bound —OH, molecular H_2O adsorbed onto lunar soil grains, or H preserved in nominally anhydrous minerals [110–112,118]. Generally, owing to the weaker solar radiation intensity, the temperature in the high-latitude region is lower than that in the low-latitude region, allowing more H from the solar wind implantation preserved in the lunar soil. The distribution of H_2O on the lunar surface, observed from the IR spectroscopy, clearly showed enrichment in the higher-latitude regions (Fig. 2; [119–121]). However, from the in situ observation with the Lunar Mineralogical Spectrometer onboard the CE-5 lander [122,123] and the study of the CE-5 returned regolith samples [124], 28.5 to 170 parts per million (ppm) of the water was witnessed and was interpreted as the contribution from the solar wind implantation or indigenous water preserved in apatites.

The source of the water on the lunar surface remains controversial. There are 3 main potential sources for the water in the lunar soil, including degassing from the lunar interior [125],

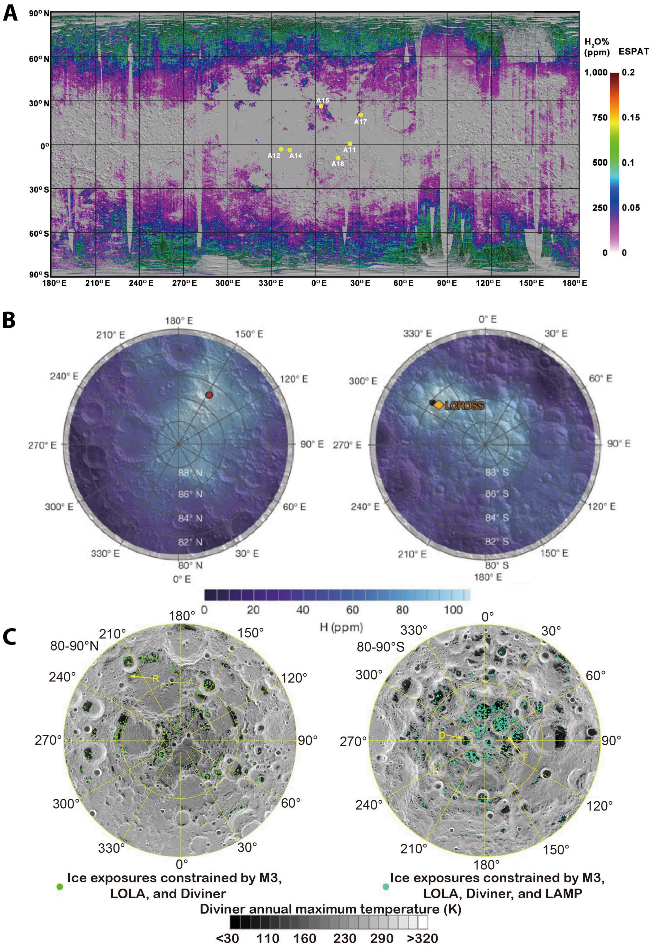

Fig. 2. Water distribution on the lunar surface. (A) Global map of effective single-particle absorption thickness (ESPAT) values (at ~2.86 μm) and estimated water contents (assuming that the irregularly shaped particles have a diameter of 60 to 80 μm) calculated from the M^3 mission data overlain on a Lunar Orbiter Laser Altimeter (LOLA) shaded-relief map. Apollo landing sites are labeled with yellow dots [119]. (B) Abundance enhancements of lunar polar hydrogen for the north and south poles measured from improved datasets from the Lunar Prospector Neutron Spectrometer using a statistics-based likelihood analysis [120]. (C) Distribution of water-ice-bearing pixels (green and cyan dots) overlain on the Diviner annual maximum temperature for the north and south poles. Ice detection results are further filtered by maximum temperature (<110 K), LOLA albedo (>0.35), and Lyman Alpha Mapping Project (LAMP) off and on band ratio (>1.2, only applicable in the south). Each dot represents an M^3 pixel, ~280 m × 280 m [121].

implantation of protons by solar wind [126–128], and accretion of water from asteroids or comets [129].

Regarding water in the interior of the Moon, some volatiles escaped from the Moon owing to the high temperature during the Moon-forming giant impact and the subsequent LMO, as well as to the relatively low gravity of the Moon [130–134]. In contrast, the frequent impacts of asteroids and comets during the late heavy bombardment could have brought water and other volatiles to the Moon [135–138], meaning that the content of water and volatiles in the interior of the Moon is uncertain. Estimations of the water content in the lunar interior have mainly been based on measurements of the water content in lunar igneous rocks and volcanic glass and on the isotopic compositions of volatile elements [139,140]. Studies of the contents and diffusion patterns of water and other volatiles in lunar volcanic glass beads revealed that the lunar interior was relatively enriched in volatiles [141–143]. However, this enrichment is frequently underestimated owing to volcanic activity and volatile degassing [130–132,144]. A series of measurements of water content in lunar soil glass beads [130], apatite in lunar mare basalts [139–141], melt inclusions [142,145], and feldspar in highland anorthosites [143] indicated the possible presence of a considerable amount of water within the lunar interior. The water contents of very low-Ti volcanic glass, melt inclusions, and crustal feldspar range from 260 to 745 ppm, 615 to 1,410 ppm, and ~2.7 ppm, respectively [145]. Based on this evidence, the estimated water content of the LMO appears to be consistent at approximately 100 ppm [144]. However, estimates of the water content of LMO based on apatite in lunar mare basalts vary widely [137]. Owing to the same stoichiometry of —OH, Cl, and F in apatite, the F content in the magma affected the apparent partition coefficient of water between the apatite and the magma, allowing for the enrichment of 1,000 ppm water in low-F apatite [141]. Additionally, during the final stages of magma differentiation, silicate–liquid immiscibility causes magma to split into Si–K-rich (felsic) and Fe-rich (Fe-basaltic) conjugate liquids, resulting in significant variations in the water content of apatite in different mesostasis pockets [146]. Despite these complexities, basing estimation on the water content and H isotopic compositions of lunar apatite can still provide a conservative estimate of the water content of the LMO, which is approximately 6 to 390 ppm [133]. Some remote sensing studies also support the presence of significant amounts of water and other volatiles in the lunar interior [122,123,147,148]. For instance, IR spectral observations of regions with thin ejecta (such as the central peaks of young impact craters, e.g., Bullialdus Crater) have shown that 0.2% to 0.6% hydroxyl groups (—OH) are necessary to account for the observed —OH peaks [147].

Like water, nonmetallic volatiles such as F, Cl, and S are gradually enriched in residual melts during magmatic evolution [142,145]. For example, lunar melt inclusions containing large amounts of water (615 to 1,410 ppm) also contain large amounts of F (50 to 78 ppm), S (612 to 877 ppm), and Cl (1.5 to 3 ppm) [145]. Degassing of these volatiles during magmatic differentiation can result in significant isotopic fractionations, which can enable estimation of the volatile content in the lunar interior. For instance, the significant chlorine isotopic fractionation observed in lunar rocks was thought to result from Cl degassing under high Cl/H ratio conditions where Cl could evaporate in the form of metal chlorides [134], thus indicating a lower water content during Cl degassing from the magma. However, others have proposed that this large chlorine isotopic variation could also be attributed to any of the following: (a) the mixing of lunar mantle sources with degassed urKREEP components (late-stage LMO residual melts thought to have been enriched in incompatible elements such as K, REEs, and P) [134,135,138], (b) isotopic fractionation induced by metamorphic processes after solidification [148], or (c) localized degassing of HCl from magma [149] rather than evaporation of Cl from a dry LMO. Metallic volatile elements (such as K, Rb, Sn, Ga, and Zn) also underwent significant degassing during the LMO stage and/or later volcanic activity, where the light isotopes of the volatiles preferentially escaped, resulting in the heavy isotopic compositions of lunar samples [150–157]. However, these metallic volatiles often have light isotopic compositions in lunar regolith, indicating that some escaped volatiles have recondensed in the lunar regolith, particularly in glasses and agglutinates ([150,154]. In addition, analyses of metallic elements and isotopic compositions on the surfaces of lunar orange glass beads have indicated the recondensation of volatiles [158]. These volatiles can also deposit in permanently shadowed regions located in the polar regions of the Moon. This phenomenon was demonstrated by the LCROSS impact experiment on the permanently shadowed crater Cabeus, which exhibited not only significant releases of water and H_2 but also substantial releases of other volatiles, such as CO, Hg, and Na [114,159]. The water and volatiles from the lunar interior can account for the lower estimates of surface water content based on remote sensing observations. For example, the water content in low-latitude regions or local water-poor areas (such as the landing site of CE-5) can be explained by the distribution of water-enriched apatite or other nominally anhydrous minerals [119,123]. However, the water from the interior of the Moon is insufficient to account for up to a few percent of the water mass observed in the permanently shadowed regions; therefore, other potential water sources must be considered [111,113].

Alternatively, impacts from meteoroids/micrometeoroids and solar wind implantation could contribute a substantial amount of H to the surface lunar soil [126–128,160]. The delivery of water and other volatiles by asteroids or comets was proposed to reconcile the conflict between degassing during the Moon-forming giant impact and the volatile-enriched lunar interior [135–138,161,162]. The H isotopic compositions of the Moon determined from comprehensive H isotopic analyses of lunar rocks (including lunar mare basalts and highland anorthosites) suggest that the Moon and the Earth have a similar water source [135]. Asteroids, represented by carbonaceous chondrites rather than comets, are likely sources of water for the Earth–Moon system [135,163]. The time of volatile addition might have been after the Moon-forming giant impact but before the formation of the lunar crust [133,140]. The isotopic compositions of other volatiles also support this hypothesis [153,157].

The solar wind implants a significant flux of protons (hydrogen) to the lunar surface and is recognized as a major water source for the lunar regolith. The H isotopic signatures of the solar wind are significantly lighter than those of the Moon, asteroids, and comets [124,126,164], making them effective indicators for identifying the solar-wind-origin hydrogen in lunar soil. Studies of the water content and the H isotopic compositions of impact-melt glasses [126] and of impact glass beads [164] from lunar regolith using secondary ion mass spectrometry revealed that a substantial amount of H was implanted into the glasses by the solar wind and was preserved in the lunar regolith. The amount of H from solar wind could contribute as much as 2.7×10^{14} kg of water to the global lunar surface [164]. In addition to glass beads, the surfaces of nominally anhydrous minerals, such as olivine and feldspar, can also retain significant amounts of H from solar wind in lunar regolith [124]. The hydrogen implanted by solar wind could serve as the dominant source of water preserved in the soil at lunar surface, subsurface, and permanently shadowed regions [109,110].

Notably, the hydrogen implanted by the solar wind into lunar glasses and minerals is predominantly present in the form of —OH rather than as water ice [165]. However, observations from LCROSS, from Chandrayaan-1's impact experiments, and from the 6-μm IR absorption band on the lunar surface confirm the presence of significant amounts of water ice on the lunar surface and in the subsurface [114,116,117,165,166], necessitating a mechanism to account for the transformation of the —OH to water ice. Furthermore, the polar distribution of water ice requires a water redistribution process on the lunar surface [109,110,125]. Water ice can be generated from —OH through photodissociation and dissociative adsorption, leading to rehydroxylation on the sunlit side or during the bombardment of micrometeorites [160,167]. Also, since the diurnal and latitudinal temperature variation is large (up to 400 K), the sublimation and condensation of volatiles on the lunar surface is significant [119,168]. Thus, the cycle of sublimation and recondensation could affect the speciation and distribution of volatiles [169]. Meanwhile, water generated from solar wind implantation and micrometeorite bombardment could be overprinted by the redistribution and absorption processes, as has been recorded in the returned samples [164,170]. The different surface temperatures could also be used to identify the water speciation and help to distinguish the source of water [123]. The heterogeneous distribution of water among different latitudes, topographies, and lithologies could be attributed to this rehydroxylation–redistribution process [121,134,171].

Cosmogenic Nuclides in Lunar Regolith

The cosmogenic nuclides present in extraterrestrial samples can provide insights into the radiation environment, shielding conditions, and space weathering history of these samples. Thus, these nuclides have various applications, such as aiding in determination of the temporal duration of meteorites' exposure to cosmic rays after leaving their parent bodies and helping to characterize the local cosmic ray flux and spectra in the solar system. Recently, metallic isotopic analyses have been widely applied in exploring the genesis and evolution of the solar system [172–179]. Nonetheless, it is crucial to acknowledge that the isotopic composition of extraterrestrial samples may be subject to alteration by cosmic ray irradiation. Consequently, to effectively use the nucleosynthesis anomalies, stable isotopic fractionation, and radioactive isotope chronology of extraterrestrial samples to deduce solar system processes, it is imperative to quantitatively assess the influence of cosmic ray effects and to correct for these effects [172,180–182]. Lunar regolith, owing to its extended exposure to cosmic ray irradiation during protracted lunar surface residence, has amassed a considerable reservoir of cosmogenic nuclides, rendering it a particularly useful subject for investigating cosmogenic nuclides [183].

Cosmogenic nuclides within lunar regolith are generated through the interaction of target elements with cosmic rays. The cosmic rays that influence the production of cosmogenic nuclides primarily consist of galactic cosmic rays (GCRs) and solar cosmic rays (SCRs). GCRs are composed of high-energy, low-flux particles/rays and exhibit a primary GCR energy spectrum spanning the range of 1 to 10^{14} MeV in interplanetary space [184]. Various compositional components of GCRs manifest similar energy spectra, with protons possessing the highest flux (≤87%), followed by helium ions (~12%); both significantly surpass the flux of heavier ions by several orders of magnitude [185,186]. SCRs are the supersonic, plasma-charged particle streams expelled from the high solar atmosphere, encompassing constituents such as protons, helium ions, and electrons [187]. In contrast to GCRs, SCRs possess an average energy near 1 MeV, exhibiting a narrower spectrum albeit with elevated flux. Additionally, SCRs encompass high-energy particle streams arising from shock acceleration propelled by SCR or coronal mass ejections [188]. Interactions between GCR particles and target nuclides within irradiated lunar regolith engender secondary particles primarily consisting of protons and neutrons. These secondary particles further interact with elements in the lunar regolith, generating additional particles until their energy is dissipated. This sequence of events yielding secondary particles is referred to as intra- and internuclear cascades [189]. Given that the energy of SCRs is lower than that of GCRs, SCR particles can only penetrate the uppermost few centimeters of lunar regolith and are incapable of generating sufficient secondary particles for the spallation or neutron capture processes. In the case of lunar regolith, SCR effects are particularly significant within the top 1 to 2 cm of the surface [183]. The flux of primary and secondary particles within the lunar samples buried in irradiated lunar regolith is contingent upon factors such as sample radius, shape, shielding depth, and chemical composition. Among these factors, sample radius and shielding depth are collectively referred to as shielding conditions or shielding parameters [189,190]. Owing to the relatively minor influence of SCRs on cosmogenic nuclides, which contribute to the production of only a few cosmogenic nuclides and are primarily confined to the uppermost few centimeters of the surface [191], greater attention has been given to the cosmogenic nuclides produced by GCR irradiation. Interactions between target nuclides and GCR particles primarily take the form of spallation reactions and thermal/epithermal neutron capture reactions. Spallation reactions involve high-energy particles (protons, neutrons, and α particles) directly interacting with target nuclides in extraterrestrial samples, inducing their fragmentation and yielding nuclei with mass numbers lower than those of the target nuclei, accompanied by the emission of other particles. Common target elements within lunar regolith include O, Mg, Al, Si, Fe, and Ni. [192]. Representative products of spallation reactions include cosmogenic noble gas isotopes such as ^{3}He, ^{21}Ne, and ^{38}Ar. Thermal and epithermal neutron capture reactions entail the capture of thermal neutrons (with energy ~0.025 eV) and epithermal neutrons (with energy in the range of 1 to 10 keV) by target nuclides, leading to the formation of new nuclei with one additional neutron. If these new nuclei are unstable, they may undergo β^- decay to form new elements. Consequently, thermal and epithermal neutron capture reactions frequently lead to transitions between neighboring isotopes of an element or between adjacent elements. The probability of this reaction is often characterized by the neutron capture cross-section. Elements with large neutron capture cross-sections include lithophile elements such as Gd, Sm, and Hf, along with more recently investigated siderophile elements such as Os, Pt, and W. These elements are often employed to indicate thermal neutron density within extraterrestrial samples [193–196].

Notably, both thermal and epithermal neutron capture reactions involve secondary neutrons generated by reactions between primary GCR particles and rocks, where the flux of these particles within irradiated objects exhibits an increasing trend and is followed by a decline with increasing shielding depth. Typically, the maximum flux occurs at a shielding depth of approximately 200 g/cm^2 [197–199], which is generally a greater depth than that of the peak spallation reaction.

Investigation of cosmogenic nuclides provides crucial constraints for understanding both the exposure history of lunar regolith samples in space and the evolutionary history of cosmic rays. Determination of the cosmic ray exposure (CRE) ages of extraterrestrial samples universally relies on the assumption of a single-stage radiation model and is calculated using the concentration of target cosmogenic nuclides and their respective production rates. The computation of cosmogenic nuclide production rates typically employs physical models, which are primarily derived from numerical simulations based on reaction cross-sections and particle flux spectra [189,200–202]. In the context of lunar samples, simulations often employ a 2π exposure geometry to assess the production rate of the cosmogenic nuclides [200,202,203]. Once the production rate information for a sample is acquired, the CRE age is determined by measuring the abundance of cosmogenic radionuclides and stable nuclides. However, it should be noted that the majority of lunar regolith samples typically have complex exposure histories [204]. The process of "gardening" has led grains within the lunar regolith to undergo repeated burial, excavation, and overall transportation in both vertical and lateral directions [1,3,205,206]. This process often leads to a lack of precise shielding information when determining the CRE age of lunar regolith samples and results in the establishment of only the lower limit of their ages [207].

The most commonly employed approach for obtaining the CRE age of lunar samples involves the determination of the stable cosmogenic noble gas nuclides (^{3}He, ^{21}Ne, ^{38}Ar, ^{83}Kr, and ^{126}Xe [204]). Because the cosmogenic noble gas nuclides are produced by the spallation of the major elements in the lunar soil, they can provide additional information on the gardening history of the lunar surface beyond fossil tracks and other isotopic indicators controlled by neutron capture, such as Sm and Gd (e.g., Apollo 15 and 16 deep drill cores [194,205,208–210]). A typical example involves the successful application of this method on ejecta to constrain the formation ages of the Cone and North Ray craters through CRE ages [207,211]. Although the widespread presence of solar wind Ne in lunar samples poses a challenge in utilizing the ^{21}Ne/^{22}Ne ratio to determine the shielding depth of samples, the diversity within noble gas isotopic systems nevertheless enables researchers to constrain the shielding depth of lunar samples using the ^{126}Xe/^{131}Xe ratio or the ^{81}Kr-Kr method [183,204,212]. Notably, Nottingham et al. [213] recently proposed a 2-stage exposure model relying on Ne isotopic compositions specifically for lunar basaltic samples and used this model to reconstruct the early exposure history of the lunar regolith. Although this method possesses certain usage limitations, it significantly reduces the sample mass (submilligram) required for determining shielding depth. Aside from the implications on constraining the gardening history of lunar soil, the cosmogenic noble gas nuclides can also provide information on the volatile contributions from solar wind [208,214–218].

Moreover, for cosmogenic nuclides with exposure ages significantly exceeding their half-lives, their radiogenic isotopic activities (the product of isotopic concentration and decay constant) would reach saturation when the radiogenic isotopic activities are approximately equal to their production rates [219]. Thus, the activities of these nuclides in static regolith are entirely dependent on the neutron flux capable of generating these nuclides within the lunar regolith layer [219–221]. The typical neutron energy required to provoke spallation reactions (such as the production reaction of ^{53}Mn and ^{26}Al [221]) is higher than that required for neutron capture reactions (such as the production reaction of ^{41}Ca and ^{60}Co [199,222]). Thus, by comparing the activities of nuclides generated by neutron capture and nuclides generated by spallation at different depths of the lunar regolith drill core, it is possible to effectively estimate variations in neutron flux within lunar regolith. Such estimation is in accord with neutron flux measured directly from the lunar regolith in the Apollo 17 lunar neutron probe experiment [223,224] (Fig. 3A). Studies of disturbances and mixing scenarios of lunar core samples using these cosmogenic nuclides reveal that in lunar regolith drill cores, such as the Apollo 15, 16, and 17 deep drill cores and drive tubes, the concentrations of short-lived nuclides (such as ^{14}C, ^{22}Na, ^{26}Al, and ^{53}Mn) are dramatically enhanced in the uppermost layer (Fig. 3C to E). This increase indicates a significant elevation in neutron flux at the surface due to the contributions of SCRs, resulting in a substantial enhancement in the saturation concentrations of short half-life nuclides [220,225–227].

Concentrations of cosmogenic nuclides can thus be used to indicate the accretion and mixing history of the lunar soil. In the steady-state CRE scenario, the activities of cosmogenic short-lived nuclides in the uppermost several centimeters are 2 to 3 times that of the deeper regions contributed from the SCR exposure, such as in the case of Apollo 16 double drive tube

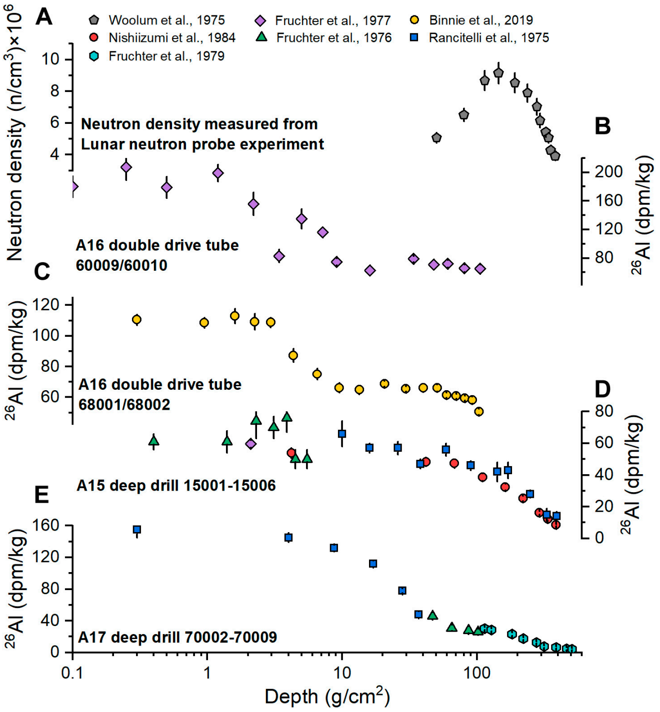

Fig. 3. Profile of neutron density and ^{26}Al activities with depth for various drill cores and drive tubes. (A) The neutron density measured from the Lunar Neutron Probe Experiment. (B to E) The profile of ^{26}Al activities in Apollo drill cores. The ^{26}Al activities are enhanced in the uppermost layer of the Apollo 16 double drive tubes [depth <10 g/cm^2; (B) and (C)] but maintain a relatively low value in the Apollo 15 deep drill core (D).

60009/60010 (Fig. 3B; [219]). If the surface layers are disturbed, the concentration of cosmogenic nuclides would become homogenized in the disturbed layers, such as in the first 3.3 g/cm^2 of the Apollo 16 double drive tube 68001/68002 [228] (Fig. 3C). In the Apollo 15 deep drill core, the concentrations of cosmogenic ^{22}Na, ^{26}Al, and ^{53}Mn are very low in the uppermost several centimeters, indicating a missing of surface regolith [229]. Nevertheless, the activity profiles of cosmogenic nuclides in the deeper regions of the Apollo deep drill core exhibit a monotonic decrease, indicating a steady-state exposure [230–232]. The absence of a significant excess of the short-lived nuclides in the uppermost regions of drill cores was also witnessed in Apollo 15 and 17 double drive tubes and the Luna 24 drill core, indicating that the upper lunar regolith in these drill cores underwent continuous or transient mixing with irradiated regolith, in contrast with the steady state in the deep layers evidenced from the monotonic decreases in concentrations of cosmogenic nuclides with depth [55,230,232–235]. In contrast, elevated but unsaturated ^{26}Al and ^{53}Mn signatures were observed in the uppermost 20 g/cm^2 of the Apollo 16 and 17 deep drill cores (Fig. 3E), indicating a complex refilling of irradiated materials to the surface [208,219,236]. When combined with decay track and thermoluminescence studies, these lunar regolith overturning histories can be further interpreted as rapid coverage of the static irradiated regolith layer with pre-irradiated ejecta in the sampling regions [205,237]. Furthermore, the different half-lives of these cosmogenic nuclides enable the estimation of temporal variations in cosmic ray flux or local solar modulation parameters by comparing the production rates of these cosmogenic nuclides. For example, the average cosmic ray flux in the last 2 Myr was consistently higher than that in the last 10 Myr [191,226,238].

Because lunar regolith is exposed to cosmic ray irradiation on the lunar surface for long periods of time, it is suitable for studying the flux of secondary thermal and epithermal neutrons. Early research focused on the nuclide ^{157}Gd (with a reaction cross-section of 25,300 barns; the barn is the unit of reaction cross-section, and 1 barn = 10^{-24} cm^2; a higher cross-section value implies a greater probability of reaction [239]). The ^{157}Gd/^{160}Gd and ^{158}Gd/^{160}Gd ratios exhibit a strong negative correlation with a slope of −1, in excellent accord with that expected from the thermal neutron capture reaction ^{157}Gd(n,γ)^{158}Gd. Combined with neutron radiation simulation experiments, ^{157}Gd/^{160}Gd and ^{158}Gd/^{160}Gd ratios have been used to calculate the neutron fluence in extraterrestrial samples [193,240]. Hidaka et al. [241] investigated the Sm (the thermal neutron capture reaction cross-section for ^{149}Sm is 40,140 barns) and the Gd isotopic composition of lunar regolith; their experiments revealed that these samples were all affected by thermal neutron capture effects, reflecting a neutron fluence on the order of 10^{15} to 10^{16} n/cm^2. Furthermore, because the thermal neutron energy required to achieve the peak production rate for ^{149}Sm and ^{157}Gd is different (^{149}Sm, 0.0973 eV; ^{157}Gd, 0.0314 eV), the ratios of ^{149}Sm/^{150}Sm and ^{157}Gd/^{158}Gd (expressed as $\varepsilon_{Sm}/\varepsilon_{Gd}$, where ε is the relative deviation of the isotopic ratio in the sample from that in the standard in parts per 10,000) can be used to infer the energy spectrum of thermal neutrons [197,241,242]. Estimations based on measurements of Sm and Gd isotopes from Apollo drill cores and those obtained through methods such as ^{10}B (n,α)^{7}Li decay tracks yield consistent neutron energy spectra [210,224,241,243,244] but are higher than the neutron energy spectra inferred from model estimation [197,245]. The $\varepsilon_{Sm}/\varepsilon_{Gd}$ ratio has also been used to trace the energy spectra of secondary neutrons in samples from different regions on the Moon [241,243]. A later study on cosmogenic Cd nuclides (^{133}Cd, which has a higher resonance absorption energy than ^{149}Sm and ^{157}Gd) in lunar drill core samples yielded a $\varepsilon_{Cd}/\varepsilon_{Sm}$ value higher than the estimation from neutron capture model under the lunar neutron flux, revealing a "harder" energy spectrum on the lunar surface [246]. Recent investigations on cosmogenic nuclides were extended to those of other rare earth elements: Dy, Er, and Yb, which are more sensitive to epithermal neutrons than Sm and Gd. Based on comparisons between concentration variations in cosmogenic nuclides of these 3 elements and those of Sm and Gd in the Apollo 15 deep drill core, the epithermal neutron flux is estimated to be approximately 10 times that of the thermal neutron flux [239]. Moreover, similar to cosmogenic noble gas nuclides and short-lived nuclides, cosmogenic nuclides of rare earth elements such as Sm and Gd can be used to identify overturning and mixing between different lunar regolith layers [209,210,244,247], constrain surface CRE ages of crater ejecta [243,248], and estimate local cosmic ray flux [244]. Compared with cosmogenic noble gas and short-lived nuclides, rare earth element nuclides are dominated by neutron capture effects, which are more sensitive to lower neutron energy levels and can reveal information from deeper-buried lunar soil, thereby providing a unique perspective for investigating the disturbance and evolutionary history of lunar regolith.

Like cosmogenic nuclides of Sm and Gd, cosmic ray radiation can significantly influence the isotopic composition of other elements within lunar regoliths such as Hf, W, Nd, and Cr [172,180–182]. The isotopic compositions of these elements play a crucial role in the study of the formation and evolutionary history of the Moon. For instance, the short-lived radioactive isotope systems ^{182}Hf-^{182}W, ^{146}Sm-^{142}Nd, and ^{53}Mn-^{53}Cr are used to determine the timing of lunar core–mantle–crust differentiation [172–176]. Additionally, isotopic anomalies of W and Cr in lunar samples are used to investigate the origin of the Moon and the accretion history of exogenous materials [177–179]. However, these isotopic compositions are susceptible to modification by cosmogenic effects. To accurately retrieve the original isotopic information from lunar samples before exposure to cosmic ray radiation, it is necessary to quantitatively assess cosmic ray effects. For example, in the ^{182}Hf-^{182}W short-lived radioactive dating system, cosmic ray radiation would cause ^{181}Ta to capture a neutron followed by β^- decay to produce ^{182}W (^{181}Ta (n,γ) ^{182}Ta (β^-,γ) ^{182}W). Given the high content of Ta in lunar samples (Ta/W = 5 [195]), the ^{182}W produced from neutron capture of ^{181}Ta dominates the total ^{182}W resulting from CRE, which, in turn, affects the accuracy of Hf-W dating results. Isotopes with large neutron capture reaction cross-sections and similar neutron capture energies to that of ^{181}Ta, such as ^{180}Hf and ^{157}Gd, have commonly been used as neutron flux indicators to correct neutron capture effects on W isotopes [172,195,196,249]. This correction strategy has also been used when calibrating other isotopic compositions of lunar samples, such as ε^{149}Sm for ε^{142}Nd and ε^{143}Nd [181], and ε^{180}Hf for ε^{176}Hf [180].

Summary and Future Prospects for Sample Returns

Lunar regolith results from space weathering and continuous gardening of lunar rocks. It not only provides clues about the interior of the Moon but also carries rich information about its space weather history, including meteoritic bombardment, solar wind implantation, and cosmic ray irradiation. Lunar regolith is a very important volatile reservoir through interaction with solar wind, asteroid addition, and volcanic degassing. Cosmic ray radiation produces nuclides through spallation and neutron capture reactions, changing the isotopic compositions of the lunar regolith, which can be used to retrieve the gardening history of the lunar regolith. A great deal of progress has been made toward understanding the composition, structure, and formation processes of lunar regolith through the accomplishments of the Chang'E mission series. Future Chang'E missions promise to shed light on the space weathering processes on the far side of the Moon (Chang'E-6), and on volatile speciation, content, and redistribution in the lunar polar region (Chang'E-7).

Acknowledgments

Funding: This work was financially supported by the National Natural Science Foundation of China (41930216 and 42241102) and the Fundamental Research Funds for the Central Universities of China (WK3410000019). L.Q. also acknowledges the support from the Tencent Foundation through the XPLORER PRIZE.
Competing interests: The authors declare that they have no competing interests.

References

1. Lucey P, Korotev RL, Gillis JJ, Taylor LA, Lawrence D, Campbell BA, Elphic R, Feldman B, Hood LL, Hunten D. Understanding the lunar surface and space-moon interactions. *Rev Mineral Geochem*. 2006;60(1):83–219.
2. Carrier WD. Lunar soil grain size distribution. *Moon*. 1973;6(3–4):250–263.
3. McKay DS, Heiken G, Basu A, Blanford G, Simon S, Reedy R, French BM, Papike J. The lunar regolith. *Lunar Sourcebook*. 1991;567:285–356.
4. Duke MB, Woo CC, Bird ML, Sellers GA, Finkelman RB. Lunar soil: Size distribution and mineralogical constituents. *Science*. 1970;167(3918):648–650.
5. Li C, Hu H, Yang M-F, Pei Z-Y, Zhou Q, Ren X, Liu B, Liu D, Zeng X, Zhang G, et al. Characteristics of the lunar samples returned by the Chang'E-5 mission. *Natl Sci Rev*. 2022;9(2):nwab188.
6. Zhang H, Zhang X, Zhang G, Dong K, Deng X, Gao X, Yang Y, Xiao Y, Bai X, Liang K, et al. Size, morphology, and composition of lunar samples returned by Chang'E-5 mission. *Sci China Phys Mechan Astron*. 2022;65:229511.
7. Gault D, Hörz F, Brownlee D, Hartung J. Mixing of the lunar regolith. In: *Lunar Science Conference*. New York: Pergamon Press Inc.; 1974. Vol 3, p. 2365–2386.
8. McKay D, Fruland R, Heiken G. Grain size and the evolution of lunar soils. In: *Lunar Science Conference*. New York: Pergamon Press Inc.; 1974. Vol 1, p. 887–906.
9. Criswell DR. Horizon-glow and motion of lunar dust. Secondary horizon-glow and motion of lunar dust. In: *Abstracts of the Lunar and Planetary Science Conference*. Houston: Lunar and Planetary Science Institute; 1972. Vol. 3, p. 163.
10. Langevin Y, Arnold JR. The evolution of the lunar regolith. *Annu Rev Earth Planet Sci*. 1977;5(1):449–489.
11. Gan H, Zhang X, Li X, Jin H, Xie L, Zou Y. Experiments on the electrostatic transport of charged Anorthite particles under electron beam irradiation. *Astrophys J*. 2022;930(1):42.
12. Gan H, Wei G, Zhang X, Xia G, Shi J. Experimental study on electrostatic migration of different mineral particles composing lunar dust under electron irradiation. *Front Astron Space Sci*. 2023;10:1213294.
13. Laul J, Lepel E. The lunar regoliths "comparative chemistry of the sampling sites". In: *Lunar and Planetary Science Conference*. Houston: Lunar and Planetary Science Institute; p. 610–612.
14. Papike JJ, Simon SB, Laul JC. The lunar regolith: Chemistry, mineralogy, and petrology. *Rev Geophys*. 1982;20(4):761–826.
15. Taylor LA, Pieters CM, Keller LP, Morris RV, McKay DS. Lunar mare soils: Space weathering and the major effects of surface-correlated nanophase Fe. *J Geophys Res Planets*. 2001;106(E11):27985–27999.
16. Zong K, Wang Z, Li J, He Q, Li Y, Becker H, Zhang W, Hu Z, He T, Cao K, et al. Bulk compositions of the Chang'E-5 lunar soil: Insights into chemical homogeneity, exotic addition, and origin of landing site basalts. *Geochim Cosmochim Acta*. 2022;335:284–296.
17. Kovach R, Watkins J, Talwani P. Apollo 16 preliminary science report. NASA SP-315; 1972. p. 10–11.
18. Renner K. Apollo 17: Preliminary Science Report; 1973.
19. Watkins JS, Kovach RL. Apollo 14 active seismic experiment. *Science*. 1972;175(4027):1244–1245.
20. Nakamura Y, Dorman J, Duennebier F, Lammlein D, Latham G. Shallow lunar structure determined from the passive seismic experiment. *Moon*. 1975;13(1–3):57–66.
21. Watkins JS, Kovach RL. Seismic investigation of the lunar regolith. *Proc Lunar Sci Conf*. 1973;4:2561.
22. Phillips RJ, Adams G, Brown W Jr, Eggleton R, Jackson P, Jordan R, Peeples W, Porcello L, Ryu J, Schaber G. The Apollo 17 lunar sounder. *Proc Lunar Sci Conf*. 1973;4:2821.
23. Xiao L, Zhu P, Fang G, Xiao Z, Zou Y, Zhao J, Zhao N, Yuan Y, Qiao L, Zhang X, et al. A young multilayered terrane of the northern Mare Imbrium revealed by Chang'E-3 mission. *Science*. 2015;347(6227):1226–1229.
24. Zhao N, Zhu P, Yang K, Yuan Y, Guo S. The preliminary processing and analysis of LPR Channel-2B data from Chang'E-3. *Sci China Phys Mechan Astron*. 2014;57(12):2346–2353.
25. Su Y, Fang G-Y, Feng J-Q, Xing S-G, Ji Y-C, Zhou B, Gao Y-Z, Li H, Dai S, Xiao Y, et al. Data processing and initial results of Chang'e-3 lunar penetrating radar. *Res Astron Astrophys*. 2014;14(12):1623.
26. Chen R, Xu Y, Xie M, Zhang L, Niu S, Bugiolacchi R. Subsurface stratification and dielectric permittivity distribution at the Chang'E-4 landing site revealed by the lunar penetrating radar. *Astron Astrophys*. 2022;664:A35.
27. Dong Z, Fang G, Zhou B, Zhao D, Gao Y, Ji Y. Properties of lunar regolith on the Moon's Farside unveiled by Chang'E-4 lunar penetrating radar. *J Geophys Res Planets*. 2021;126(6):e2020JE006564.
28. Feng Y, Chen S, Tong X, Wang C, Li P, Xi M, Xiao C. Exploring the lunar Regolith's thickness and dielectric properties using band-limited impedance at Chang'E-4 landing site. *J Geophys Res Planets*. 2023;128(3):e2022JE007540.
29. Li C, Su Y, Pettinelli E, Xing S, Ding C, Liu J, Ren X, Lauro SE, Soldovieri F, Zeng X, et al. The Moon's farside shallow subsurface structure unveiled by Chang'E-4 lunar penetrating radar. *Sci Adv*. 2020;6(9):eaay6898.
30. Huang J, Xiao Z, Flahaut J, Martinot M, Head J, Xiao X, Xie M, Xiao L. Geological characteristics of Von Kármán crater, northwestern south pole-Aitken Basin: Chang'E-4

landing site region. *J Geophys Res Planets*. 2018;123(7): 1684–1700.
31. Su Y, Wang R, Deng X, Zhang Z, Zhou J, Xiao Z, Ding C, Li Y, Dai S, Ren X, et al. Hyperfine structure of regolith unveiled by Chang'E-5 lunar regolith penetrating radar. *IEEE Trans Geosci Remote Sens*. 2022;60:1–14.
32. Bart GD, Nickerson RD, Lawder MT, Melosh HJ. Global survey of lunar regolith depths from LROC images. *Icarus*. 2011;215(2):485–490.
33. Di K, Sun S, Yue Z, Liu B. Lunar regolith thickness determination from 3D morphology of small fresh craters. *Icarus*. 2016;267:12–23.
34. Fa W, Liu T, Zhu MH, Haruyama J. Regolith thickness over sinus iridum: Results from morphology and size-frequency distribution of small impact craters. *J Geophys Res Planets*. 2014;119(8):1914–1935.
35. Quaide WL, Oberbeck VR. Thickness determinations of the lunar surface layer from lunar impact craters. *J Geophys Res*. 1968;73(16):5247–5270.
36. Wilcox B, Robinson M, Thomas P, Hawke B. Constraints on the depth and variability of the lunar regolith. *Meteorit Planet Sci*. 2005;40(5):695–710.
37. Fa W, Jin Y. Analysis of microwave brightness temperature of lunar surface and inversion of regolith layer thickness: Primary results of Chang-E 1 multi-channel radiometer observation. *Sci China Inf Sci*. 2010;53(1):168–181.
38. Fa W, Wieczorek MA. Regolith thickness over the lunar nearside: Results from earth-based 70-cm Arecibo radar observations. *Icarus*. 2012;218(2):771–787.
39. Kobayashi T, Kim JH, Lee SR, Araki H, Ono T. Simultaneous observation of lunar radar sounder and laser altimeter of Kaguya for lunar regolith layer thickness estimate. *IEEE Geosci Remote Sens Lett*. 2010;7(3):435–439.
40. Ono T, Kumamoto A, Nakagawa H, Yamaguchi Y, Oshigami S, Yamaji A, Kobayashi T, Kasahara Y, Oya H. Lunar radar sounder observations of subsurface layers under the nearside Maria of the moon. *Science*. 2009;323(5916):909–912.
41. Shkuratov YG, Bondarenko NV. Regolith layer thickness mapping of the moon by radar and optical data. *Icarus*. 2001;149(2):329–338.
42. Zhou M, Zhou J, Zhang X, Wang F. Inversion of microwave brightness temperature data for estimating lunar regolith thickness. *Int J Appl Electromagn Mech*. 2010;33(3–4): 1041–1048.
43. Gong X, Jin YQ. Microwave brightness temperature of cratered lunar surface and inversions of the physical temperature profile and thickness of regolith layer. *Radio Sci*. 2012;47(1):1–11.
44. Venkatraman J, Paige DA. Statistical estimates of rock-free lunar regolith thickness from diviner. *Planet Space Sci*. 2023;229:Article 105662.
45. Williams JP, Bandfield J, Paige D, Powell T, Greenhagen B, Taylor S, Hayne P, Speyerer E, Ghent R, Costello E. Lunar cold spots and crater production on the moon. *J Geophys Res Planets*. 2018;123(9):2380–2392.
46. Melosh HJ. *Impact cratering: A geologic process.* New York: Oxford University Press; 1989.
47. Melosh HJ. *Planetary surface processes*. Cambridge (UK): Cambridge University Press; 2011.
48. Kring D. *Meteor crater—The world's first proven asteroid impact crater.* Boulder (CO): Geological Society of America Abstracts; 2023.
49. Osinski GR, Tornabene LL, Grieve RAF. Impact ejecta emplacement on terrestrial planets. *Earth Planet Sci Lett*. 2011;310(3–4):167–181.
50. Arnold JR. A Monte Carlo model for the gardening of the lunar regolith. *Moon*. 1975;13(1–3):159–172.
51. Crawford IA, Fagents SA, Joy KH, Rumpf ME. Lunar palaeoregolith deposits as recorders of the galactic environment of the solar system and implications for astrobiology. *Earth Moon Planet*. 2010;107(1):75–85.
52. Shuster DL, Balco G, Cassata WS, Fernandes VA, Garrick-Bethell I, Weiss BP. A record of impacts preserved in the lunar regolith. *Earth Planet Sci Lett*. 2010;290(1–2):155–165.
53. Lin H, Lin Y, Yang W, He Z, Hu S, Wei Y, Xu R, Zhang J, Liu X, Yang J, et al. New insight into lunar regolith-forming processes by the lunar rover Yutu-2. *Geophys Res Lett*. 2020;47(14):e2020GL087949.
54. Wilhelms DE, McCauley JF, Trask NJ. *The geologic history of the Moon*. Reston: United States Geological Survey; 1987.
55. Fruchter JS, Rancitelli LA, Evans JC, Perkins RW. Lunar surface processes and cosmic ray histories over the past several million years. *Proc Lunar Planet Sci Conf*. 1978;2019–2032.
56. Crider DH, Vondrak RR. Space weathering of ice layers in lunar cold traps. *Adv Space Res*. 2003;31(11):2293–2298.
57. Costello ES, Ghent RR, Lucey PG. The mixing of lunar regolith: Vital updates to a canonical model. *Icarus*. 2018;314:327–344.
58. Oberbeck VR, Quaide WL, Mahan M, Paulson J. Monte Carlo calculations of lunar regolith thickness distributions. *Icarus*. 1973;19(1):87–107.
59. Quaide W, Oberbeck V. Development of the mare regolith: Some model considerations. *Moon*. 1975;13(1–3):27–55.
60. Hörz F. Impact cratering and regolith dynamics. *Phys Chem Earth*. 1977;10:3–15.
61. Fischer EM, Pieters CM. Lunar surface aluminum and iron concentration from Galileo solid state imaging data, and the mixing of mare and highland materials. *J Geophys Res Planets*. 1995;100(E11):23279–23290.
62. Li L, Mustard JF. On lateral mixing efficiency of lunar regolith. *J Geophys Res Planets*. 2005;110(E11):E11002.
63. Richardson JE. Cratering saturation and equilibrium: A new model looks at an old problem. *Icarus*. 2009;204(2): 697–715.
64. Huang YH, Minton DA, Hirabayashi M, Elliott JR, Richardson JE, Fassett CI, Zellner NEB. Heterogeneous impact transport on the moon. *J Geophys Res Planets*. 2017;122(6):1158–1180.
65. Liu T, Michael G, Engelmann J, Wünnemann K, Oberst J. Regolith mixing by impacts: Lateral diffusion of basin melt. *Icarus*. 2019;321:691–704.
66. Di K, Liu Z, Liu B, Wan W, Peng M, Wang Y, Gou S, Yue Z, Xin X, Jia M. Chang'e-4 lander localization based on multi-source data. *J Remote Sens*. 2019;23(1):177–184.
67. Gou S, Yue Z, Di K, Cai Z, Liu Z, Niu S. Absolute model age of lunar Finsen crater and geologic implications. *Icarus*. 2021;354:Article 114046.
68. Kneissl T, van Gasselt S, Neukum G. Map-projection-independent crater size-frequency determination in GIS environments—New software tool for ArcGIS. *Planet Space Sci*. 2011;59(11–12):1243–1254.
69. Jia M, Di K, Yue Z, Liu B, Wan W, Niu S, Liu J, Cheng W, Lin Y. Multi-scale morphologic investigation of craters in the Chang'e-4 landing area. *Icarus*. 2021;355:Article 114164.

70. McGetchin TR, Settle M, Head JW. Radial thickness variation in impact crater ejecta: Implications for lunar basin deposits. *Earth Planet Sci Lett*. 1973;20(2):226–236.
71. Sharpton VL. Outcrops on lunar crater rims: Implications for rim construction mechanisms, ejecta volumes and excavation depths. *J Geophys Res Planets*. 2014;119(1):154–168.
72. Hirabayashi M, Howl BA, Fassett CI, Soderblom JM, Minton DA, Melosh HJ. The role of breccia lenses in regolith generation from the formation of small, simple craters: Application to the Apollo 15 landing site. *J Geophys Res Planets*. 2018;123(2):527–543.
73. Krishna N, Kumar PS. Impact spallation processes on the moon: A case study from the size and shape analysis of ejecta boulders and secondary craters of Censorinus crater. *Icarus*. 2016;264:274–299.
74. Neukum G, Ivanov BA, Hartmann WK. Cratering records in the inner solar system in relation to the lunar reference system. *Space Sci Rev*. 2001;96:55–86.
75. Neukum G. Meteoritenbombardement und datierung planetarer oberflachen [dissertation]. Ludwig-Maximilians-Univ; 1983.
76. Soderblom LA. A model for small-impact erosion applied to the lunar surface. *J Geophys Res*. 1970;75(14):2655–2661.
77. Fassett CI, Thomson BJ. Crater degradation on the lunar maria: Topographic diffusion and the rate of erosion on the moon. *J Geophys Res Planets*. 2014;119(10):2255–2271.
78. Shi K, Yue Z, Di K, Liu J, Dong Z. The gardening process of lunar regolith by small impact craters: A case study in Chang'E-4 landing area. *Icarus*. 2022;377:Article 114908.
79. Pieters CM, Noble SK. Space weathering on airless bodies. *J Geophys Res Planets*. 2016;121(10):1865–1884.
80. Noble SK, Pieters CM. *Sol Syst Res*. 2003;37(1):31–35.
81. Ballouz R-L, Baresi N, Crites ST, Kawakatsu Y, Fujimoto M. Surface refreshing of Martian moon Phobos by orbital eccentricity-driven grain motion. *Nat Geosci*. 2019;12(4):229–234.
82. Hiroi T, Abe M, Kitazato K, Abe S, Clark BE, Sasaki S, Ishiguro M, Barnouin-Jha OS. Developing space weathering on the asteroid 25143 Itokawa. *Nature*. 2006;443(7107):56–58.
83. Kaluna HM, Masiero JR, Meech KJ. Space weathering trends among carbonaceous asteroids. *Icarus*. 2016;264:62–71.
84. Noguchi T, Matsumoto T, Miyake A, Igami Y, Haruta M, Saito H, Hata S, Seto Y, Miyahara M, Tomioka N, et al. A dehydrated space-weathered skin cloaking the hydrated interior of Ryugu. *Nat Astron*. 2023;7(2):170–181.
85. Chapman CR. Space weathering of asteroid surfaces. *Annu Rev Earth Planet Sci*. 2004;32(1):539–567.
86. Pieters CM, Taylor LA, Noble SK, Keller LP, Hapke B, Morris RV, Allen CC, McKay DS, Wentworth S. Space weathering on airless bodies: Resolving a mystery with lunar samples. *Meteorit Planet Sci*. 2000;35(5):1101–1107.
87. Noble SK, Pieters CM, Taylor LA, Morris RV, Allen CC, McKay DS, Keller LP. The optical properties of the finest fraction of lunar soil: Implications for space weathering. *Meteorit Planet Sci*. 2001;36(1):31–42.
88. Lucey P, Noble S. Experimental test of a radiative transfer model of the optical effects of space weathering. *Icarus*. 2008;197(1):348–353.
89. Lucey PG, Riner MA. The optical effects of small iron particles that darken but do not redden: Evidence of intense space weathering on mercury. *Icarus*. 2011;212(2):451–462.
90. Keller LP, McKay DS. The nature and origin of rims on lunar soil grains. *Geochim Cosmochim Acta*. 1997;61(11):2331–2341.
91. Gargaud M, Amils R. *Encyclopedia of astrobiology*. Springer Science & Business Media; 2011.
92. Li C, Guo Z, Li Y, Tai K, Wei K, Li X, Liu J, Ma W. Impact-driven disproportionation origin of nanophase iron particles in Chang'e-5 lunar soil sample. *Nat Astron*. 2022;6(10):1156–1162.
93. Noble SK, Pieters CM, Keller LP. An experimental approach to understanding the optical effects of space weathering. *Icarus*. 2007;192(2):629–642.
94. Gu L, Chen Y, Xu Y, Tang X, Lin Y, Noguchi T, Li J. Space weathering of the Chang'e-5 lunar sample from a mid-high latitude region on the moon. *Geophys Res Lett*. 2022;49(7):e2022GL097875.
95. Burgess KD, Stroud RM. Glassy with a chance of nanophase iron: Space weathering of lunar soil as observed with aberration-corrected scanning transmission electron microscopy. *Microscopy Today*. 2017;25(3):32–39.
96. Utt KL, Ogliore RC, Bechtel HA, Gillis-Davis JJ, Jolliff BL. Detecting sub-micron space weathering effects in lunar grains with synchrotron infrared nanospectroscopy. *J Geophys Res Planets*. 2021;126(9):e2021JE006921.
97. Yang Y, Jiang T, Liu Y, Xu Y, Zhang H, Tian HC, Yang W, Zou Y. A micro mid-infrared spectroscopic study of Chang'e-5 sample. *J Geophys Res Planets*. 2022;127(8):e2022JE007453.
98. Sasaki S, Hiroi T, Nakamura K, Hamabe Y, Kurahashi E, Yamada M. Simulation of space weathering by nanosecond pulse laser heating: Dependence on mineral composition, weathering trend of asteroids and discovery of nanophase iron particles. *Adv Space Res*. 2002;29(5):783–788.
99. Matsuoka M, Nakamura T, Hiroi T, Okumura S, Sasaki S. Space weathering simulation with low-energy laser irradiation of Murchison CM chondrite for reproducing micrometeoroid bombardments on C-type asteroids. *Astrophys J*. 2020;890(2):L23.
100. Weber I, Stojic AN, Morlok A, Reitze MP, Markus K, Hiesinger H, Pavlov SG, Wirth R, Schreiber A, Sohn M, et al. Space weathering by simulated micrometeorite bombardment on natural olivine and pyroxene: A coordinated IR and TEM study. *Earth Planet Sci Lett*. 2020;530:Article 115884.
101. Marchi S, Brunetto R, Magrin S, Lazzarin M, Gandolfi D. Space weathering of near-earth and main belt silicate-rich asteroids: Observations and ion irradiation experiments. *Astron Astrophys*. 2005;443(3):769–775.
102. Loeffler MJ, Dukes CA, Baragiola RA. Irradiation of olivine by 4 keV He^+: Simulation of space weathering by the solar wind. *J Geophys Res Planets*. 2009;114:E3.
103. Fulvio D, Brunetto R, Vernazza P, Strazzulla G. Space weathering of Vesta and V-type asteroids: New irradiation experiments on HED meteorites. *Astron Astrophys*. 2012;537:L11.
104. Trang D, Lucey PG. Improved space weathering maps of the lunar surface through radiative transfer modeling of Kaguya multiband imager data. *Icarus*. 2019;321:307–323.
105. Wang Z, Wu Y, Blewett DT, Cloutis EA, Zheng Y, Chen J. Submicroscopic metallic iron in lunar soils estimated from the in situ spectra of the Chang'E-3 mission. *Geophys Res Lett*. 2017;44(8):3485–3492.
106. Gou S, Yue Z, Di K, Wan W, Liu Z, Liu B, Peng M, Wang Y, He Z, Xu R. In situ spectral measurements of space weathering by Chang'e-4 rover. *Earth Planet Sci Lett*. 2020;535:Article 116117.

107. Wu X, Liu Y, Yang Y, Guo D, Du J, Li S, Lin H, Fu X, Xiao Z, Xu Y, et al. Mineralogy and regolith maturity at the Chang'E-5 landing site inferred from the lunar mineralogical spectrometer. *Earth Planet Sci Lett*. 2022;594:Article 117747.
108. Canup RM. Dynamics of lunar formation. *Annu Rev Astron Astrophys*. 2004;42(1):441–475.
109. Lucey PG. A lunar water world. *Science*. 2009;326(5952):531–532.
110. Pieters CM, Goswami JN, Clark RN, Annadurai M, Boardman J, Buratti B, Combe JP, Dyar MD, Green R, Head JW, et al. Character and spatial distribution of OH/H_2O on the surface of the moon seen by M^3 on Chandrayaan-1. *Science*. 2009;326(5952):568–572.
111. Sunshine JM, Farnham TL, Feaga LM, Groussin O, Merlin F, Milliken RE, A'Hearn MF. Temporal and spatial variability of lunar hydration as observed by the deep impact spacecraft. *Science*. 2009;326(5952):565–568.
112. Clark RN. Detection of adsorbed water and hydroxyl on the moon. *Science*. 2009;326(5952):562–564.
113. Colaprete A, Schultz P, Heldmann J, Wooden D, Shirley M, Ennico K, Hermalyn B, Marshall W, Ricco A, Elphic RC, et al. Detection of water in the LCROSS ejecta plume. *Science*. 2010;330(6003):463–468.
114. Gladstone GR, Hurley DM, Retherford KD, Feldman PD, Pryor WR, Chaufray J-Y, Versteeg M, Greathouse TK, Steffl AJ, Throop H, et al. LRO-LAMP observations of the LCROSS impact plume. *Science*. 2010;330(6003):472–476.
115. Hayne PO, Greenhagen BT, Foote MC, Siegler MA, Vasavada AR, Paige DA. Diviner lunar radiometer observations of the LCROSS impact. *Science*. 2010;330(6003):477–479.
116. Sridharan R, Ahmed SM, Pratim Das T, Sreelatha P, Pradeepkumar P, Naik N, Supriya G. "Direct" evidence for water (H_2O) in the sunlit lunar ambience from CHACE on MIP of Chandrayaan I. *Planet Space Sci*. 2010;58(6):947–950.
117. Mitrofanov IG, Sanin AB, Boynton WV, Chin G, Garvin JB, Golovin D, Evans LG, Harshman K, Kozyrev AS, Litvak ML, et al. Hydrogen mapping of the lunar south pole using the LRO neutron detector experiment LEND. *Science*. 2010;330(6003):483–486.
118. Pathak S, Dagar AK, Bhattacharya S, Moitra H, Chauhan M, Gupta S. Geological insights into lunar floor-fractured crater atlas. *Icarus*. 2021;360:Article 114374.
119. Li S, Milliken RE. Water on the surface of the moon as seen by the moon mineralogy mapper: Distribution, abundance, and origins. *Sci Adv*. 2017;3(9):Article e1701471.
120. Siegler M, Miller R, Keane J, Laneuville M, Paige D, Matsuyama I, Lawrence D, Crotts A, Poston M. Lunar true polar wander inferred from polar hydrogen. *Nature*. 2016;531(7595):480–484.
121. Li S, Lucey PG, Milliken RE, Hayne PO, Fisher E, Williams J-P, Hurley DM, Elphic RC. Direct evidence of surface exposed water ice in the lunar polar regions. *Proc Natl Acad Sci USA*. 2018;115(36):8907–8912.
122. Lin H, Li S, Xu R, Liu Y, Wu X, Yang W, Wei Y, Lin Y, He Z, Hui H, et al. In situ detection of water on the moon by the Chang'E-5 lander. *Sci Adv*. 2022;8(1):eabl9174.
123. Liu J, Liu B, Ren X, Li C, Shu R, Guo L, Yu S, Zhou Q, Liu D, Zeng X, et al. Evidence of water on the lunar surface from Chang'E-5 in-situ spectra and returned samples. *Nat Commun*. 2022;13(1):3119.
124. Zhou C, Tang H, Li X, Zeng X, Mo B, Yu W, Wu Y, Zeng X, Liu J, Wen Y. Chang'E-5 samples reveal high water content in lunar minerals. *Nat Commun*. 2022;13(1):5336.
125. Paige DA, Siegler MA, Zhang JA, Hayne PO, Foote EJ, Bennett KA, Vasavada AR, Greenhagen BT, Schofield JT, McCleese DJ, et al. Diviner lunar radiometer observations of cold traps in the Moon's south polar region. *Science*. 2010;330(6003):479–482.
126. Liu Y, Guan Y, Zhang Y, Rossman GR, Eiler JM, Taylor LA. Direct measurement of hydroxyl in the lunar regolith and the origin of lunar surface water. *Nat Geosci*. 2012;5(11):779–782.
127. Bandfield JL, Poston MJ, Klima RL, Edwards CS. Widespread distribution of OH/H_2O on the lunar surface inferred from spectral data. *Nat Geosci*. 2018;11(3):173–177.
128. Benna M, Hurley DM, Stubbs TJ, Mahaffy PR, Elphic RC. Lunar soil hydration constrained by exospheric water liberated by meteoroid impacts. *Nat Geosci*. 2019;12(5):333–338.
129. Feldman WC, Maurice S, Binder AB, Barraclough BL, Elphic RC, Lawrence DJ. Fluxes of fast and epithermal neutrons from lunar prospector: Evidence for water ice at the lunar poles. *Science*. 1998;281(5382):1496–1500.
130. Saal AE, Hauri EH, Cascio ML, Van Orman JA, Rutherford MC, Cooper RF. Volatile content of lunar volcanic glasses and the presence of water in the Moon's interior. *Nature*. 2008;454(7201):192–195.
131. Saal AE, Hauri EH, Van Orman JA, Rutherford MJ. Hydrogen isotopes in lunar volcanic glasses and melt inclusions reveal a carbonaceous chondrite heritage. *Science*. 2013;340(6138):1317–1320.
132. Saal A, Hauri E. Large sulfur isotope fractionation in lunar volcanic glasses reveals the magmatic differentiation and degassing of the moon. *Sci Adv*. 2021;7(9):eabe4641.
133. Tartèse R, Anand M, McCubbin FM, Elardo SM, Shearer CK, Franchi IA. Apatites in lunar KREEP basalts: The missing link to understanding the H isotope systematics of the moon. *Geology*. 2014;42(4):363–366.
134. Sharp ZD, Shearer CK, McKeegan KD, Barnes JD, Wang YQ. The chlorine isotope composition of the moon and implications for an anhydrous mantle. *Science*. 2010;329(5995):1050–1053.
135. Hauri EH, Saal AE, Rutherford MJ, Van Orman JA. Water in the Moon's interior: Truth and consequences. *Earth Planet Sci Lett*. 2015;409:252–264.
136. Greenwood JP, Itoh S, Sakamoto N, Warren P, Taylor L, Yurimoto H. Hydrogen isotope ratios in lunar rocks indicate delivery of cometary water to the moon. *Nat Geosci*. 2011;4(2):79–82.
137. Barnes JJ, Tartèse R, Anand M, McCubbin FM, Franchi IA, Starkey NA, Russell SS. The origin of water in the primitive moon as revealed by the lunar highlands samples. *Earth Planet Sci Lett*. 2014;390:244–252.
138. Barnes JJ, Kring DA, Tartèse R, Franchi IA, Anand M, Russell SS. An asteroidal origin for water in the moon. *Nat Commun*. 2016;7(1):11684.
139. McCubbin FM, Steele A, Hauri EH, Nekvasil H, Yamashita S, Hemley RJ. Nominally hydrous magmatism on the moon. *Proc Natl Acad Sci USA*. 2010;107(25):11223–11228.
140. Boyce JW, Liu Y, Rossman GR, Guan Y, Eiler JM, Stolper EM, Taylor LA. Lunar apatite with terrestrial volatile abundances. *Nature*. 2010;466(7305):466–469.
141. Boyce JW, Tomlinson SM, McCubbin FM, Greenwood JP, Treiman AH. The lunar apatite paradox. *Science*. 2014;344(6182):400–402.

142. Chen Y, Zhang Y, Liu Y, Guan Y, Eiler J, Stolper EM. Water, fluorine, and sulfur concentrations in the lunar mantle. *Earth Planet Sci Lett*. 2015;427:37–46.
143. Hui H, Peslier AH, Zhang Y, Neal CR. Water in lunar anorthosites and evidence for a wet early moon. *Nat Geosci*. 2013;6(3):177–180.
144. Robinson KL, Taylor GJ. Heterogeneous distribution of water in the moon. *Nat Geosci*. 2014;7(6):401–408.
145. Hauri EH, Weinreich T, Saal AE, Rutherford MC, Van Orman JA. High pre-eruptive water contents preserved in lunar melt inclusions. *Science*. 2011;333(6039):213–215.
146. Pernet-Fisher JF, Howarth GH, Liu Y, Chen Y, Taylor LA. Estimating the lunar mantle water budget from phosphates: Complications associated with silicate-liquid-immiscibility. *Geochim Cosmochim Acta*. 2014;144:326–341.
147. Klima R, Cahill J, Hagerty J, Lawrence D. Remote detection of magmatic water in Bullialdus crater on the moon. *Nat Geosci*. 2013;6(9):737–741.
148. Potts NJ, Barnes JJ, Tartèse R, Franchi IA, Anand M. Chlorine isotopic compositions of apatite in Apollo 14 rocks: Evidence for widespread vapor-phase metasomatism on the lunar nearside ~4 billion years ago. *Geochim Cosmochim Acta*. 2018;230:46–59.
149. Gargano A, Sharp Z, Shearer C, Simon JI, Halliday A, Buckley W. The Cl isotope composition and halogen contents of Apollo-return samples. *Proc Natl Acad Sci USA*. 2020;117(38):23418–23425.
150. Wang K, Jacobsen SB. Potassium isotopic evidence for a high-energy giant impact origin of the moon. *Nature*. 2016;538(7626):487–490.
151. Tian Z, Jolliff BL, Korotev RL, Fegley B, Lodders K, Day JMD, Chen H, Wang K. Potassium isotopic composition of the moon. *Geochim Cosmochim Acta*. 2020;280:263–280.
152. Pringle EA, Moynier F. Rubidium isotopic composition of the earth, meteorites, and the moon: Evidence for the origin of volatile loss during planetary accretion. *Earth Planet Sci Lett*. 2017;473:62–70.
153. Pringle EA, Moynier F, Beck P, Paniello R, Hezel DC. The origin of volatile element depletion in early solar system material: Clues from Zn isotopes in chondrules. *Earth Planet Sci Lett*. 2017;468:62–71.
154. Wang X, Fitoussi C, Bourdon B, Fegley B, Charnoz S. Tin isotopes indicative of liquid–vapour equilibration and separation in the moon-forming disk. *Nat Geosci*. 2019;12(9):707–711.
155. Paniello RC, Day JMD, Moynier F. Zinc isotopic evidence for the origin of the moon. *Nature*. 2012;490(7420):376–379.
156. Kato C, Moynier F, Valdes MC, Dhaliwal JK, Day JMD. Extensive volatile loss during formation and differentiation of the moon. *Nat Commun*. 2015;6(1):7617.
157. Kato C, Moynier F. Gallium isotopic evidence for the fate of moderately volatile elements in planetary bodies and refractory inclusions. *Earth Planet Sci Lett*. 2017;479:330–339.
158. Herzog GF, Moynier F, Albarède F, Berezhnoy AA. Isotopic and elemental abundances of copper and zinc in lunar samples, Zagami, Pele's hairs, and a terrestrial basalt. *Geochim Cosmochim Acta*. 2009;73(19):5884–5904.
159. Schultz PH, Hermalyn B, Colaprete A, Ennico K, Shirley M, Marshall WS. The LCROSS cratering experiment. *Science*. 2010;330(6003):468–472.
160. Zhu C, Crandall PB, Gillis-Davis JJ, Ishii HA, Bradley JP, Corley LM, Kaiser RI. Untangling the formation and liberation of water in the lunar regolith. *Proc Natl Acad Sci USA*. 2019;116(23):11165–11170.
161. Wang Z, Becker H. Ratios of S, Se and Te in the silicate earth require a volatile-rich late veneer. *Nature*. 2013;499(7458):328–331.
162. Marty B, Altwegg K, Balsiger H, Bar-Nun A, Bekaert DV, Berthelier JJ, Bieler A, Briois C, Calmonte U, Combi M, et al. Xenon isotopes in 67P/Churyumov-Gerasimenko show that comets contributed to Earth's atmosphere. *Science*. 2017;356(6342):1069–1072.
163. Braukmüller N, Wombacher F, Funk C, Münker C. Earth's volatile element depletion pattern inherited from a carbonaceous chondrite-like source. *Nat Geosci*. 2019;12(7):564–568.
164. He H, Ji J, Zhang Y, Hu S, Lin Y, Hui H, Hao J, Li R, Yang W, Tian H, et al. A solar wind-derived water reservoir on the moon hosted by impact glass beads. *Nat Geosci*. 2023;16(4):294–300.
165. Honniball C, Lucey P, Li S, Shenoy S, Orlando T, Hibbitts C, Hurley D, Farrell W. Molecular water detected on the sunlit moon by SOFIA. *Nat Astron*. 2021;5(2):121–127.
166. Jones BM, Aleksandrov A, Hibbitts CA, Orlando TM. Thermal evolution of water and hydrogen from Apollo lunar regolith grains. *Earth Planet Sci Lett*. 2021;571: Article 117107.
167. Jones BM, Aleksandrov A, Hibbitts K, Dyar MD, Orlando TM. Solar wind-induced water cycle on the moon. *Geophys Res Lett*. 2018;45(20):10–959.
168. Mandt KE, Mousis O, Hurley D, Bouquet A, Retherford KD, Magaña LO, Luspay-Kuti A. Exogenic origin for the volatiles sampled by the lunar CRater observation and sensing satellite impact. *Nat Commun*. 2022;13:642.
169. Williams J-P, Paige DA, Greenhagen BT, Sefton-Nash E. The global surface temperatures of the moon as measured by the diviner lunar radiometer experiment. *Icarus*. 2017;283: 300–325.
170. Milliken RE, Li S. Remote detection of widespread indigenous water in lunar pyroclastic deposits. *Nat Geosci*. 2017;10(8):561–565.
171. Jones BM, Aleksandrov A, Dyar MD, Hibbitts CA, Orlando TM. Investigation of water interactions with Apollo lunar regolith grains. *J Geophys Res Planets*. 2020;125(6): e2019JE006147.
172. Kruijer TS, Kleine T, Fischer-Gödde M, Sprung P. Lunar tungsten isotopic evidence for the late veneer. *Nature*. 2015;520(7548):534–537.
173. Touboul M, Puchtel IS, Walker RJ. Tungsten isotopic evidence for disproportional late accretion to the earth and moon. *Nature*. 2015;520(7548):530–533.
174. Borg LE, Connelly JN, Boyet M, Carlson RW. Chronological evidence that the moon is either young or did not have a global magma ocean. *Nature*. 2011;477(7362):70–72.
175. McLeod CL, Brandon AD, Armytage RMG. Constraints on the formation age and evolution of the moon from ^{142}Nd–^{143}Nd systematics of Apollo 12 basalts. *Earth Planet Sci Lett*. 2014;396:179–189.
176. Lugmair GW, Shukolyukov A. Early solar system timescales according to ^{53}Mn-^{53}Cr systematics. *Geochim Cosmochim Acta*. 1998;62(16):2863–2886.
177. Archer GJ, Budde G, Worsham EA, Stracke A, Jackson MG, Kleine T. Origin of ^{182}W anomalies in Ocean Island basalts. *Geochem Geophys Geosyst*. 2023;24(2):e2022GC010688.

178. Dauphas N, Burkhardt C, Warren PH, Fang-Zhen T. Geochemical arguments for an earth-like moon-forming impactor. *Philos Trans R Soc A Math Phys Eng Sci*. 2024;2014(372):20130244.
179. Dauphas N. The isotopic nature of the Earth's accreting material through time. *Nature*. 2017;541(7638):521–524.
180. Sprung P, Scherer EE, Upadhyay D, Leya I, Mezger K. Non-nucleosynthetic heterogeneity in non-radiogenic stable Hf isotopes: Implications for early solar system chronology. *Earth Planet Sci Lett*. 2010;295(1–2):1–11.
181. Sprung P, Kleine T, Scherer EE. Isotopic evidence for chondritic Lu/Hf and Sm/Nd of the moon. *Earth Planet Sci Lett*. 2013;380:77–87.
182. Mougel B, Moynier F, Göpel C. Chromium isotopic homogeneity between the moon, the earth, and enstatite chondrites. *Earth Planet Sci Lett*. 2018;481:1–8.
183. Wieler R. Cosmic-ray-produced noble gases in meteorites. *Rev Mineral Geochem*. 2002;47(1):125–170.
184. Fisk LA, Gloeckler G. Particle acceleration in the heliosphere: Implications for astrophysics. *Space Sci Rev*. 2012;173 (1–4):433–458.
185. Simpson JA. Elemental and isotopic composition of the galactic cosmic rays. *Annu Rev Nucl Part Sci*. 1983;33(1):323–382.
186. Nordheim TA, Jasinski JM, Hand KP. Galactic cosmic-ray bombardment of Europa's surface. *Astrophys J*. 2019;881(2):L29.
187. Gloeckler G, Balsiger H, Bürgi A, Bochsler P, Fisk LA, Galvin AB, Geiss J, Gliem F, Hamilton DC, Holzer TE, et al. The solar WIND and suprathermal ion composition investigation on the WIND spacecraft. *Space Sci Rev*. 1995;71(1–4):79–124.
188. Reames DV. Particle acceleration at the Sun and in the heliosphere. *Space Sci Rev*. 1999;90:413–491.
189. Ammon K, Masarik J, Leya I. New model calculations for the production rates of cosmogenic nuclides in iron meteorites. *Meteorit Planet Sci*. 2009;44(4):485–503.
190. Eugster O, Herzog G, Marti K, Caffee M. Irradiation records, cosmic-ray exposure ages, and transfer times of meteorites. *Meteor Early Solar Syst*. 2006;II(943):829–851.
191. Li Y, Zhang X, Dong W, Ren Z, Dong T, Xu A. Simulation of the production rates of cosmogenic nuclides on the moon based on Geant4. *J Geophys Res Space Physics*. 2017;122(2):1473–1486.
192. Leya I, Begemann F, Weber HW, Wieler R, Michel R. Simulation of the interaction of galactic cosmic ray protons with meteoroids: On the production of ^{3}H and light noble gas isotopes in isotropically irradiated thick gabbro and iron targets. *Meteorit Planet Sci*. 2004;39(3):367–386.
193. Eugster O, Tera F, Burnett DS, Wasserburg GJ. Neutron capture effects in Gd from the Norton County meteorite. *Earth Planet Sci Lett*. 1970;7(5):436–440.
194. Hidaka H, Ebihara M, Yoneda S. Isotopic study of neutron capture effects on Sm and Gd in chondrites. *Earth Planet Sci Lett*. 2000;180(1-2):29–37.
195. Leya I, Wieler R, Halliday AN. The influence of cosmic-ray production on extinct nuclide systems. *Geochim Cosmochim Acta*. 2003;67(3):529–541.
196. Kruijer TS, Fischer-Gödde M, Kleine T, Sprung P, Leya I, Wieler R. Neutron capture on Pt isotopes in iron meteorites and the Hf–W chronology of core formation in planetesimals. *Earth Planet Sci Lett*. 2013;361:162–172.
197. Lingenfelter R, Canfield E, Hampel V. The lunar neutron flux revisited. *Earth Planet Sci Lett*. 1972;16(3):355–369.
198. Spergel M, Reedy R, Lazareth O, Levy P, Slatest L. Cosmogenic neutron-capture-produced nuclides in stony meteorites. *J Geophys Res Solid Earth*. 1986;91(B4):483–494.
199. Nishiizumi K, Fink D, Klein J, Middleton R, Masarik J, Reedy R, Arnold J. Depth profile of41Ca in an Apollo 15 drill core and the low-energy neutron flux in the moon. *Earth Planet Sci Lett*. 1997;148(3–4):545–552.
200. Hohenberg C, Marti K, Podosek F, Reedy R, Shirck J. Comparisons between observed and predicted cosmogenic noble gases in lunar samples. *Proc Lunar Planet Sci Conf*. 1978;2:2311–2344.
201. Leya I, Masarik J. Cosmogenic nuclides in stony meteorites revisited. *Meteorit Planet Sci*. 2009;44(7):1061–1086.
202. Leya I, Neumann S, Wieler R, Michel R. The production of cosmogenic nuclides by galactic cosmic-ray particles for 2π exposure geometries. *Meteorit Planet Sci*. 2001;36(11): 1547–1561.
203. Regnier S, Hohenberg C, Marti K, Reedy R. Predicted versus observed cosmic-ray-produced noble gases in lunar samples-improved KR production ratios. *Proc Lunar Planet Sci Conf*. 1979;2:1565–1586.
204. Eugster O. Cosmic-ray exposure ages of meteorites and lunar rocks and their significance. *Geochemistry*. 2003;63(1):3–30.
205. Morris RV. In situ reworking (gardening) of the lunar surface: Evidence from the Apollo cores. *Proc Lunar Planet Sci Conf*. 1978;2:1801–1811.
206. Borg J, Chaumont J, Jouret C, Langevin Y, Maurette M. Solar wind radiation damage in lunar dust grains and the characteristics of the ancient solar wind. *Proc Conf Ancient Sun*. 1980;431–461.
207. Curran N, Nottingham M, Alexander L, Crawford I, Füri E, Joy K. A database of noble gases in lunar samples in preparation for mass spectrometry on the moon. *Planet Space Sci*. 2020;182:Article 104823.
208. Bogard DD, Nyquist LE, Hirsch WC, Moore DR. Trapped solar and cosmogenic noble gas abundances in Apollo 15 and 16 deep drill samples. *Earth Planet Sci Lett*. 1973;21(1):52–69.
209. Russ GP III, Burnett D, Wasserburg G. Lunar neutron stratigraphy. *Earth Planet Sci Lett*. 1972;15(2):172–186.
210. Curtis DB, Wasserburg GJ. Stratigraphic processes in the lunar regolith—Additional insight from neutron fluence measurements on bulk soils and lithic fragments from the deep drill cores. *Proc Lunar Planet Sci Conf*. 1977;3:3575–3593.
211. Füri E, Zimmermann L, Hiesinger H. Noble gas exposure ages of samples from cone and north ray craters: Implications for the recent lunar cratering chronology. *Meteorit Planet Sci*. 2021;56(11):2047–2061.
212. Eugster O, Geiss J, Krähenbühl U, Niedermann S. Noble gas isotopic composition, cosmic ray exposure history, and terrestrial age of the meteorite Allan Hills A81005 from the moon. *Earth Planet Sci Lett*. 1986;78(2–3):139–147.
213. Nottingham MC, Stuart FM, Chen B, Zurakowska M, Gilmour JD, Alexander L, Crawford IA, Joy KH. Complex burial histories of Apollo 12 basaltic soil grains derived from cosmogenic noble gases: Implications for local regolith evolution and future in situ investigations. *Meteorit Planet Sci*. 2022;57(3):603–634.
214. Agrawal JK, Gopalan K, Rao MN. Solar wind and cosmogenic rare gases in Luna 16 and 20 soils and their correlation with cosmic ray produced fossil tracks in lunar samples. *Pramana*. 1974;3(3):176–185.

215. Will P, Busemann H, Riebe MEI, Maden C. Indigenous noble gases in the Moon's interior. *Sci Adv*. 2022;8(31):eabl4920.
216. Eugster O, Grögler N, Mendia MD, Eberhardt P, Geiss J. Trapped solar wind noble gases and exposure age of Luna 16 lunar fines. *Geochim Cosmochim Acta*. 1973;37(9):1991–2003.
217. Padia JT, Rao MN, Venkatesan TR. Cosmogenic and trapped rare gases in Luna-24 drill core samples. *Moon Planets*. 1979;20(4):423–438.
218. Bogard DD, Hirsch WC, Nyquist LE. Noble gases in Apollo 17 fines: Mass fractionation effects in trapped Xe and Kr. *Proc Lunar Planet Sci Conf*. 1974;(2):1975–2003.
219. Fruchter J, Rancitelli L, Laul J, Perkins R. Lunar regolith dynamics based on analysis of the cosmogenic radionuclides Na-22, Al-26, and Mn-53. *Proc Lunar Planet Sci Conf*. 1977;3595–3605.
220. Nishiizumi K, Murrell MT, Arnold JR. ^{53}Mn profiles in four Apollo surface cores. *J Geophys Res Solid Earth*. 1983;88:S01.
221. Nishiizumi K, Klein J, Middleton R, Arnold JR. ^{26}Al depth profile in Apollo 15 drill core. *Earth Planet Sci Lett*. 1984;70(2):164–168.
222. Wahlen M, Finkel RC, Imamura M, Kohl CP, Arnold JR. ^{60}Co in lunar samples. *Earth Planet Sci Lett*. 1973;19(3):315–320.
223. Mesick KE, Feldman WC, Coupland DDS, Stonehill LC. Benchmarking Geant4 for simulating galactic cosmic ray interactions within planetary bodies. *Earth Space Sci*. 2018;5(7):324–338.
224. Woolum DS, Burnett D, Furst M, Weiss J. Measurement of the lunar neutron density profile. *Moon*. 1975;12:231–250.
225. Jull AJT, Cloudt S, Donahue DJ, Sisterson JM, Reedy RC, Masarik J. 14C depth profiles in Apollo 15 and 17 cores and lunar rock 68815. *Geochim Cosmochim Acta*. 1998;62(17):3025–3036.
226. Rancitelli L, Fruchter J, Felix W, Perkins R, Wogman N. Cosmogenic isotope production in Apollo deep-core samples. *Proc Lunar Planet Sci Conf*. 1975;2:1891–1899.
227. Fruchter J, Reeves J, Rancitelli L, Perkins R. History of the Apollo 17 deep drill string during the past few million years. *Proc Lunar Planet Sci Conf*. 1979;2:1243–1251.
228. Binnie SA, Nishiizumi K, Welten KC, Caffee MW, Hoffmeister D. Lunar surface processes inferred from cosmogenic radionuclides in Apollo 16 double drive core 68002/68001. *Geochim Cosmochim Acta*. 2019;244:336–351.
229. Fruchter JS, Rancitelli LA, Perkins RW. Recent and long-term mixing of the lunar regolith based on ^{22}Na and ^{26}Al measurements in Apollo 15, 16, and 17 deep drill stems and drive tubes. *Proc Lunar Planet Sci Conf*. 1976;1:27–39.
230. Imamura M, Finkel RC, Wahlen M. Depth profile of ^{53}Mn in the lunar surface. *Earth Planet Sci Lett*. 1973;20(1):107–112.
231. Imamura M, Nishiizumi K, Honda M, Finkel R, Arnold J, Kohl C. Depth profiles of Mn-53 in lunar rocks and soils. *Proc Lunar Planet Sci Conf*. 1974;2:2093–2103.
232. Nishiizumi K, Arnold J, Elmore D, Tubbs L, Cole G, Newman D. Measurements of cosmic ray produced ^{53}Mn and ^{10}Be in lunar cores. *Proc Lunar Planet Sci Conf*. 1982;596–597.
233. Emrich P, Jurina V, Povinec P. Cosmogenic ^{22}Na and ^{26}Al and track studies in Luna 16, 20 and 24 samples. *Bull Astronom Institutes Czech*. 1984;35:253.
234. Povinec P, Lavrukhina A, Ustinova G. Cosmogenic ^{22}Na and ^{26}Al in Luna 24 drill Core soil samples. *Proc Lunar Planet Sci Conf*. 1982;22:629–630.
235. Povinec P, Lavrukhina A, Ustinova G. Na-22 and Al-26 in Luna 24 samples. *Int Cosmic Ray Conf*. 1983;2:385–388.
236. Evans JC, Fruchter JS, Reeves JH, Rancitelli LA, Perkins RW. Recent depositional history of Apollo 16 and 17 cores. *Proc Lunar Planet Sci Conf*. 1980;1497–1509.
237. Crozaz G, Plachy A. Origin of the Apollo 17 deep drill coarse-grained layer. *Proc Lunar Planet Sci Conf*. 1976;7: 123–131.
238. Frolov D, Pavlov A, Ostryakov V, Konstantinov A, Vasilyev G, Kudryavtsev I, Dergachev V. Reconstruction of solar activity based on ^{14}C and other isotope profiles in lunar regolith. *J Phys Conf Ser*. 2021;2103(1):Article 012007.
239. Hidaka H, Mizutani Y, Yoneda S. Estimation of thermal and epithermal neutron fluences at the lunar surface from isotopic compositions of rare earth elements. *Astrophys J*. 2020;904(2):183.
240. Lugmair G, Marti K. Neutron capture effects in lunar gadolinium and the irradiation histories of some lunar rocks. *Earth Planet Sci Lett*. 1971;13(1):32–42.
241. Hidaka H, Ebihara M, Yoneda S. Neutron capture effects on samarium, europium, and gadolinium in Apollo 15 deep drill-core samples. *Meteorit Planet Sci*. 2000;35(3):581–589.
242. Hidaka H, Sakuma K, Nishiizumi K, Yoneda S. Isotopic evidence for MULTI-stage cosmic-ray exposure histories of lunar meteorites: Long residence on the moon and short transition to the earth. *Astron J*. 2017;153(6):274.
243. Curtis DB, Wasserburg G. Transport and erosional processes in the Taurus-Littrow Valley-inferences from neutron fluences in surface soils. *Proc Lunar Planet Sci Conf*. 1977;3:3045–3057.
244. Hidaka H, Yoneda S. Sm and Gd isotopic shifts of Apollo 16 and 17 drill stem samples and their implications for regolith history. *Geochim Cosmochim Acta*. 2007;71(4):1074–1086.
245. DePaolo D, McCulloch M, Papanastassiou D, Huneke J, Wasserburg G. Ages, evolution and neutron effects of Luna 24 samples. *Proc Lunar Planet Sci Conf*. 1978;244–246.
246. Sands DG, De Laeter JR, Rosman KJR. Measurements of neutron capture effects on cd, Sm and Gd in lunar samples with implications for the neutron energy spectrum. *Earth Planet Sci Lett*. 2001;186(3–4):335–346.
247. Curtis DB, Wasserburg GJ. Apollo 17 neutron stratigraphy sedimentation and mixing in the lunar regolith. *Moon*. 1975;13(1–3):185–227.
248. Russ GP, Burnett DS, Lingenfelter RE, Wasserburg GJ. Neutron capture on ^{149}Sm in lunar samples. *Earth Planet Sci Lett*. 1971;13(1):53–60.
249. Qin L, Dauphas N, Horan MF, Leya I, Carlson RW. Correlated cosmogenic W and Os isotopic variations in Carbo and implications for Hf–W chronology. *Geochim Cosmochim Acta*. 2015;153:91–104.
250. Cooper MR, Kovach RL, Watkins JS. Lunar near-surface structure. *Rev Geophys*. 1974;12(3):291–308.